Ore Geology Reviews 140 (2022) 104588

Contents lists available at ScienceDirect

Ore Geology Reviews

journal homepage: www.elsevier.com/locate/oregeorev

An improved gas extraction model during stepwise crushing: New perspectives on fluid geochronology and geochemistry

Ming Xiao [a,b,c], Ying-De Jiang [a,b,*], Hua-Ning Qiu [d,e,*], Yue Cai [f], Wan-Feng Zhang [a,b]

[a] State Key Laboratory of Isotope Geochemistry, Guangzhou Institute of Geochemistry, Chinese Academy of Sciences, Guangzhou 510640, China
[b] CAS Center for Excellence in Deep Earth Science, Guangzhou 510640, China
[c] Department of Earth Sciences, The University of Hong Kong, Pokfulam Road, Hong Kong, China
[d] Key Laboratory of Tectonics and Petroleum Resources (China University of Geosciences), Ministry of Education, Wuhan 430074, China
[e] School of Earth Resources, China University of Geosciences, Wuhan 430074, China
[f] Amont-Doherty Earth Observatory of Columbia University, 61 Rt. 9W, Palisades, NY 10964, USA

ARTICLE INFO

Keywords:
Gentle stepwise crushing
Fluid inclusions
Gas extraction model
Source identification
Bulk analysis

ABSTRACT

Trapped fossil fluids in mineral-hosted fluid inclusions preserve pivotal information on the evolution of paleo geological systems, particularly the hydrothermal mineralization systems. However, identification of the sources of the extracted gases during bulk analysis of fluid inclusions is challenging because multiple generations, types, and phases of fluid inclusions may exist in the same mineral. To better identify the gas sources during stepwise crushing we report an improved gas extraction model of fluid inclusions. Stepwise extracted gases from fluid inclusions in quartz and cassiterite were measured with a quadrupole mass spectrometer and compared with Raman analysis of different types of secondary (SFIs) and primary (PFIs) fluid inclusions. We found that H_2O-poor and CO_2-rich gases with elevated CO_2/CH_4 ratios, H_2O and formamide-rich gases, and CH_4-rich gases were extracted sequentially during stepwise crushing. Such compositional variations of the released gases suggest that the extraction of fluid inclusions starts from SFIs with high vapor-filling degrees (*f*) and CO_2-bearing tri-phase high-*f* fluid inclusions, which is followed by large liquid-rich SFIs and mid-sized high-*f* PFIs that are rich in CO_2 and formamide, and ends with small CH_4-rich low-*f* PFIs. These findings suggest that the degassing pattern of hydrothermal minerals during stepwise crushing is mostly governed by the physicochemical characteristics of the fluid inclusions, in particular, their vapor-filling degrees, sizes, compositions (which can lead to different inner pressures and densities), and associations with micro-cracks. This updated model of gas release patterns strengthens the theoretical basis for differentiating and identifying the sources of gases extracted during stepwise crushing experiments, which is key to understanding the fluid geochronology and geochemistry of hydrothermal deposits with multi-stage hydrothermal evolution in general.

1. Introduction

Through heat and elemental exchanges between the earth's surface and its interior, hydrothermal activities play important roles in many geological processes and are crucial for the formation of ore deposits worldwide (Gamo and Glasby, 2003; Pirajno, 2008; Lowell et al., 2014; Simmons, 2021). As such, hydrothermal fluids trapped in inclusions, especially in primary fluid inclusions, could contribute to our understanding of a geologic system, particularly the ore-forming systems (Roedder, 1997; Yardley and Bodnar, 2014). In particular, gas compositions of fluid inclusions provide unique insights into the metal mineralization processes and the provenance, evolution as well as physical and chemical conditions of the ore-forming fluids (Andrawes and Gibson, 1979; Bergman and Dubessy, 1984; Norman and Sawkins, 1987; Blamey, 2012; Buikin et al., 2014).

1.1. Traditional extraction methods for gas composition analysis of fluid inclusion populations

Thermal decrepitation (Scott, 1948; Alderton et al., 1982) and

* Corresponding authors at: State Key Laboratory of Isotope Geochemistry, Guangzhou Institute of Geochemistry, Chinese Academy of Sciences, Guangzhou 510640, China (Ying-De Jiang); Key Laboratory of Tectonics and Petroleum Resources (China University of Geosciences), Ministry of Education, Wuhan 430074, China (Hua-Ning Qiu).
E-mail addresses: jiangyd@gig.ac.cn (Y.-D. Jiang), huaningqiu@cug.edu.cn (H.-N. Qiu).

https://doi.org/10.1016/j.oregeorev.2021.104588
Received 26 August 2021; Received in revised form 10 November 2021; Accepted 14 November 2021
Available online 19 November 2021

mechanical crushing (Andrawes and Gibson, 1979; Andrawes et al., 1984; Kelley et al., 1986) are two of the most common ways to extract gases from fluid inclusion populations for gas composition analysis using mass spectrometry or gas chromatography.

Thermal decrepitation is often regarded as an effective way to successively extract secondary and primary fluid inclusions, at lower and higher temperatures, respectively. However, in addition to the trapping temperatures, decrepitation behaviors also depend on physicochemical characteristics including size, shape, distribution, density, and composition of the fluid inclusions and the mechanical properties of the host minerals (Bodnar et al., 2003; Campione et al., 2015). For example, compared with large fluid inclusions, tiny ones can sustain larger internal pressures, and higher temperatures are therefore required to decrepitate them. This has been demonstrated by heating experiments of quartz minerals (Kelley et al., 1986; Hall and Bodnar, 1989) and mantle xenoliths (Hopp and Trieloff, 2005) where they found that a large proportion of gases were released above 800 °C or higher. Moreover, the heating process may also lead to the formation of secondary neonate inclusions (less than a few μm in size) from re-equilibration of larger fluid inclusions, which could have distinct compositions from the precursor inclusions (Pecher, 1981; Tarantola et al., 2012). Significant release of these tiny fluid inclusions at a higher temperature would interfere with analytical results of the larger primary fluid inclusions.

Additionally, heating experiments of quartz have shown that pseudosecondary gaseous inclusions (e.g., CO_2-rich inclusions) could be decrepitated at lower temperatures than similar-sized secondary aqueous ones (e.g., H_2O-rich inclusions) due to their higher inner pressures (Partamies and Poutiainen, 2001). This finding suggests that thermal decrepitation is not always an effective way to distinguish gases from different fluid inclusion generations. Moreover, high-temperature reactions would generate significant amounts of additional gas species, making the qualification and quantification of gases less reliable (Landis et al., 2005; Blamey, 2012).

Mechanical crushing is a better way to extract mineral-hosted fluid inclusions since limited high-temperature reactions develop during extraction. However, most traditional crushers are designed based on the original stainless-steel piston-cylinder apparatus (Andrawes et al., 1984; Matsumoto et al., 2001) and screw-type crusher (Stuart et al., 1994). These crushers are commonly associated with heavy crushing strengths, and as a consequence, gases from different sources, e.g., secondary fluid inclusions, primary fluid inclusions as well as mineral micro-cracks, lattice, and impurities could be simultaneously extracted during crushing, especially when prolonged crushing processes are applied with a large number of crushing (Scarsi, 2000; Villa, 2001; Kendrick et al., 2006). On the contrary, if the samples are only crushed with a small number of strokes, e.g., several to tens of strokes, small fluid inclusions, especially the micron-sized primary fluid inclusions, would not be fully extracted (Norman and Sawkins, 1987; Blamey, 2012).

More importantly, a common weakness of these traditional extraction methods is that they cannot distinguish different fluid inclusion populations as they would be extracted simultaneously (Villa, 2001; Landis et al., 2005; Blamey, 2012). For example, significant interferences from secondary fluid inclusions could lead to geologically meaningless data if the gases were assumed to be derived only from the primary fluid inclusions (Villa, 2001; Qiu et al., 2002). This problem hinders the understanding of the thermal evolution of a given geological system. Improvements upon existing extraction methods are therefore urgently needed.

1.2. Progressive extraction using gentle stepwise crushing technique

Stepwise crushing technique has been applied to gas composition analysis of fluid inclusions and mantle rocks for decades (Sarda et al., 1985; Staudacher et al., 1989; Trieloff et al., 2000; Hopp et al., 2004; Buikin et al., 2005; Buikin et al., 2014). This method permits progressive extraction of fluid inclusions based on their generation, and as such, studies of volatile and isotope compositions and geochronology of different generations of fluid inclusions become possible (Qiu and Jiang, 2007; Jiang et al., 2012; Buikin et al., 2016; Bai et al., 2018a; Xiao et al., 2019). For example, when combined with $^{40}Ar/^{39}Ar$ geochronology, stepwise crushing has shown great potential in obtaining the formation ages of both secondary and primary fluid inclusions (Qiu and Jiang, 2007; Jiang et al., 2012; Xiao et al., 2019; Bai et al., 2013, 2018a).

It has long been noted that stepwise crushing preferentially extracted large secondary fluid inclusions along micro-cracks in the initial crushing stage while gases from smaller primary ones were mainly extracted in the final crushing stage (Stuart and Turner, 1992; Trieloff et al., 1997; Qiu and Wijbrans, 2006; Qiu and Jiang, 2007; Jiang et al., 2012; Bai et al., 2018a). When the extraction technique was connected to a quadrupole mass spectrometer (QMS), many authors have observed significant compositional differences in gases released from different crushing stages (Fang et al., 2018; Liu et al., 2018; Xiao et al., 2021), which further supports the hypothesis that different populations of fluid inclusions are gradually extracted during stepwise crushing. Recently, we have applied the QMS-stepwise crushing technique to measure common gases (e.g., CO_2, CH_4, H_2O, and organic species) of a few major groups of fluid inclusions in cassiterite, wolframite, and quartz with relatively simple phase behaviors. Along with irradiation-derived argon isotopes of these samples, these results allowed us to summarize a first-order gas release pattern of fluid inclusions during stepwise crushing (Xiao et al., 2019). This was an important step towards understanding the overall degassing behavior of fluid inclusions in hydrothermal minerals during stepwise crushing.

1.3. The main purpose of this study

While the earlier stepwise crushing experiments cited above have built a framework that greatly improved our understanding of fluid inclusion gas release behaviors during stepwise crushing (Qiu and Jiang, 2007; Jiang et al., 2012; Bai et al., 2013, 2018a; Xiao et al., 2019), these pilot studies focused on fluid inclusions in hydrothermal minerals with a simple hydrothermal history. In reality, most hydrothermal minerals have much more complex geologic histories. Taken an ordinary ore deposit as an example, it could have undergone multiple types of fluid processes and multiple episodes of hydrothermal disturbances during its geological evolution, which usually lead to the formation of multiple generations and phases of fluid inclusions with much more complicated characteristics than those used to establish the existing gas release patterns.

In this study, based on detailed micropetrography and Raman spectroscopy of fluid inclusions, we coupled gentle stepwise crushing experiments with QMS gas composition analysis on minerals with more complex hydrothermal history to improve the gas release pattern proposed by Xiao et al. (2019). It is our hope that the updated model of gas release patterns established here could be generally applicable for minerals from most hydrothermal systems when they are stepwise crushed and analyzed for volatile, isotope, and noble gas compositions.

The Yaogangxian tungsten deposit is the type of hydrothermal deposit that underwent multi-stages of hydrothermal disturbances. Intense late-stage hydrothermal overprints likely generated multiple populations of fluid inclusions in ore and gangue minerals as documented in many previous studies (Cao et al., 2009; Dong et al., 2011; Xiao et al., 2019; Xiao et al., 2021). Additionally, ore minerals and gangue mineral quartz could have undergone different fluid processes during their precipitation as fluid immiscibility appear to have only affected quartz that formed later (Xiao et al., 2021). All these hydrothermal processes should generate distinct fluid inclusion characteristics in ore and quartz minerals. This is the type of situation we want to address in the current study through the identification of common gas release behaviors for multi-generations/phases of fluid inclusions during a stepwise crushing procedure.

2. Geological setting and sample descriptions

2.1. Geological setting

The South China Craton, situated in the southeastern part of Eurasian, comprises the Yangtze Block in the northwest and the Cathaysia Block in the southeast (Fig. 1a and b). As one of the most important polymetallic metallogenic provinces in the world, the South China Craton is well known for its metal mineral resources with multiple word-class W, Sn, and Sb deposits and many important rare-metals, Cu, Hg, As, Pb, Zn, Au, and Ag deposits (Hua et al., 2003; Mao et al., 2011; Mao et al., 2013; Yuan et al., 2019). The Nanling Region (111°–117°E, 23°20′–26°40′N, Fig. 1c), located at the central-southern part of the South China Craton, forms the famous Nanling polymetallic minerogenic belt, which is characterized by widespread and multiple-aged granitoids and associated W, Sn, and rare-metal mineralization (Shu, 2007; Chen et al., 2013). Most of the W, Sn, and rare-metal deposits in this belt formed during Middle–Late Jurassic (*ca.* 160–150 Ma, Hua et al., 2003; Mao et al., 2013). The polymetallic mineralization in this belt is generally spatially and genetically associated with the regional Late Mesozoic granitic plutons that are thought to be related to the subduction of the Paleo-Pacific oceanic plate (Shu, 2007).

The Yaogangxian tungsten deposit is a world-class tungsten deposit located in the center of the Nanling polymetallic minerogenic belt in the northwestern Cathaysia Block. It consists of a dominant quartz-vein-type wolframite deposit and a small-scale skarn-type scheelite deposit. In the mining district, thick Cambrian *meta*-sandstone and slate succession is unconformably overlain by Devono–Carboniferous sandstone and limestone as well as the overlying younger Triassic–Jurassic sandstone-dominated sequence (Fig. 1d) (Chen, 1992; Zhu et al., 2015). The Yaogangxian composite granitic pluton consists of highly differentiated S-type granites, which intruded Devonian and Cambrian strata with wolframite-bearing ore bodies commonly developed along the contact zone between them (Fig. 1d) (Lin et al., 1986; Chen, 1988). Crystallization ages of the granites are constrained by zircon U–Pb ages at 161–155 Ma (Li et al., 2011; Li et al., 2020). The timing of wolframite mineralization broadly falls within a range of 163–153 Ma, which was constrained by Re–Os, $^{40}Ar/^{39}Ar$ stepwise heating and crushing, and *in-situ* LA-ICP MS U–Pb dating (Peng et al., 2006; Wang et al., 2010; Deng et al., 2019; Xiao et al., 2019; Li et al., 2020). The spatial and temporal

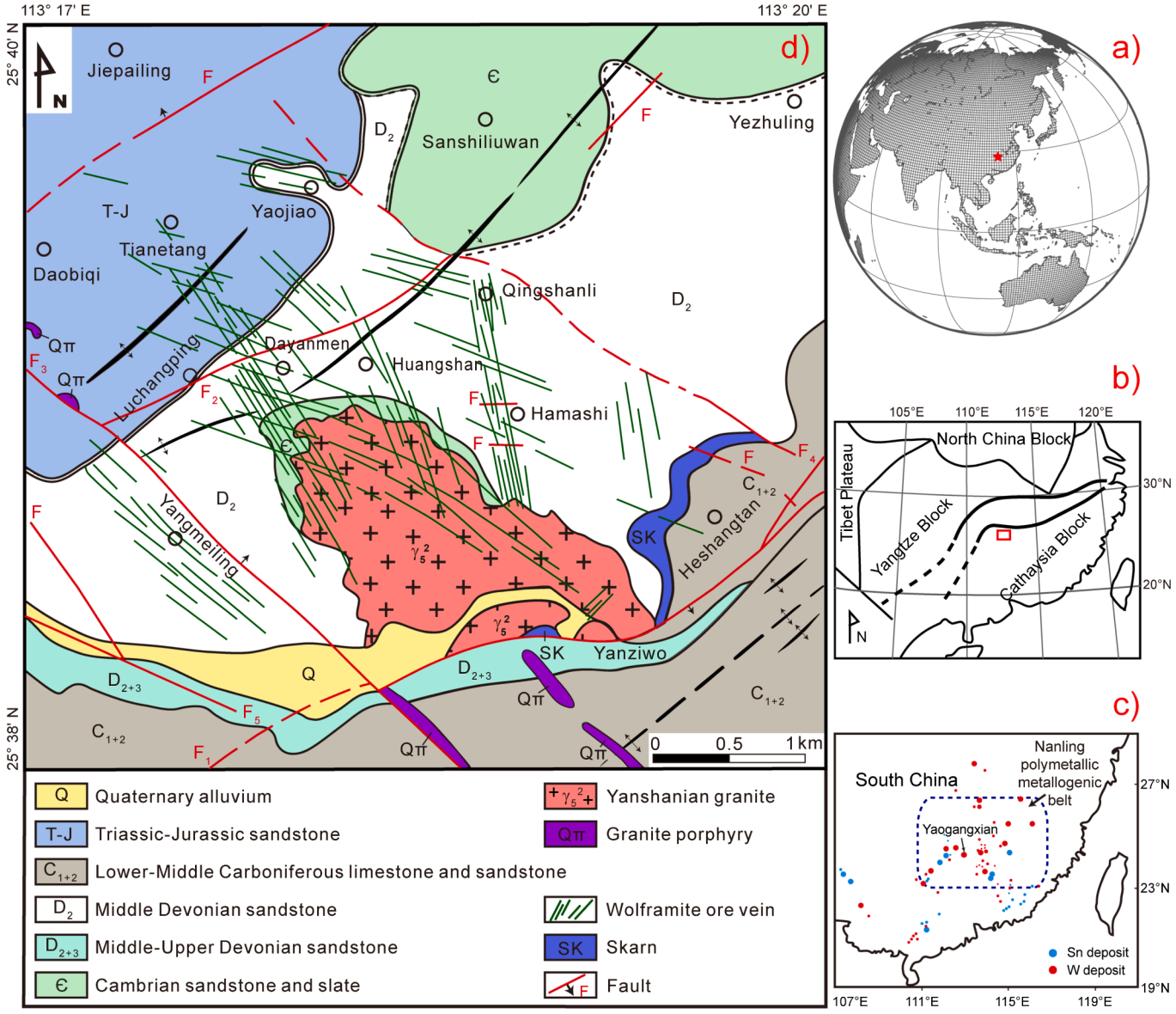

Fig. 1. Simplified geological map showing the location (a–c) and geological characteristics (d, modified after Peng et al. (2006) and Zhu et al. (2015)) of the Yaogangxian tungsten deposit. Important W-Sn ore deposits in South China are also indicated (after Mao et al. (2011)).

associations between the granites and the wolframite-bearing ore bodies indicate a potential genetic link between them (e.g., Li et al., 2011; Li et al., 2020).

2.2. Sample description

Two ore-bearing quartz vein samples with multiple associated minerals were studied. Sample 13YGX06 contains quartz, muscovite, wolframite, arsenopyrite, pyrite, chalcopyrite, and minor cassiterite (Fig. 2a and d). Sample 13YGX32 contains wolframite, quartz, muscovite, cassiterite, and abundant sulfides such as chalcopyrite, pyrite, arsenopyrite, and sphalerite, together with some calcite and K-feldspar (Fig. 2b–c and e–h). The complex mineral assemblages of these samples indicate multi-stage hydrothermal events during or after ore-formation. Additionally, fluid immiscibility occurred in later-formed quartz samples that are associated with sulfides, especially chalcopyrite that usually forms in late- or post-mineralization stage (e.g., Fig. 2i, Xiao et al., 2021), which resulted in multi-phase fluid inclusions coexisting in the quartz. These different hydrothermal processes should, therefore, lead to complicated and distinct characteristics of the fluid inclusions in the associated ore mineral cassiterite and gangue mineral quartz, which makes them good test subjects for revealing the impact of phases of fluid inclusions on extraction. Detailed studies of these minerals allow us to construct a more systematic model of gas release patterns of fluid inclusions for common hydrothermal minerals through gentle stepwise crushing.

3. Analytical methods

3.1. Compositional analysis of individual fluid inclusions by Raman spectroscopy

A series of ~100 μm thick double-polished fluid inclusion wafers were prepared for the quartz and cassiterite samples for laser Raman compositional analysis using a Renishaw InVia Reflex micro-Raman spectrometer, equipped with an Ar^{+} ion laser (514.5 nm), at State Key Laboratory of Ore Deposit Geochemistry, Institute of Geochemistry, Chinese Academy of Sciences (IGCAS). The resolution was ± 1 cm^{-1}.

Several common gas species were identified: CO_2 = 1386–1388 cm^{-1}, CH_4 = 2916–2918 cm^{-1}, N_2 = 2327–2329 cm^{-1}. Formamide [CH_3NO] was identified by Raman peaks at 1430–1390 cm^{-1} (amide III band (C–N) stretching), 1640–1620 cm^{-1} (amide II band (N–H) vibration, 1620–1585 cm^{-1} for non-associated molecule), 1650 ± 20 cm^{-1} (amide I band (C=O) stretching, 1685 ± 15 cm^{-1} for non-associated molecule), 1669 cm^{-1} (C=O stretching vibration of primary amide), and/or 1607 cm^{-1} (formamide dissolving in water) (Puranik and

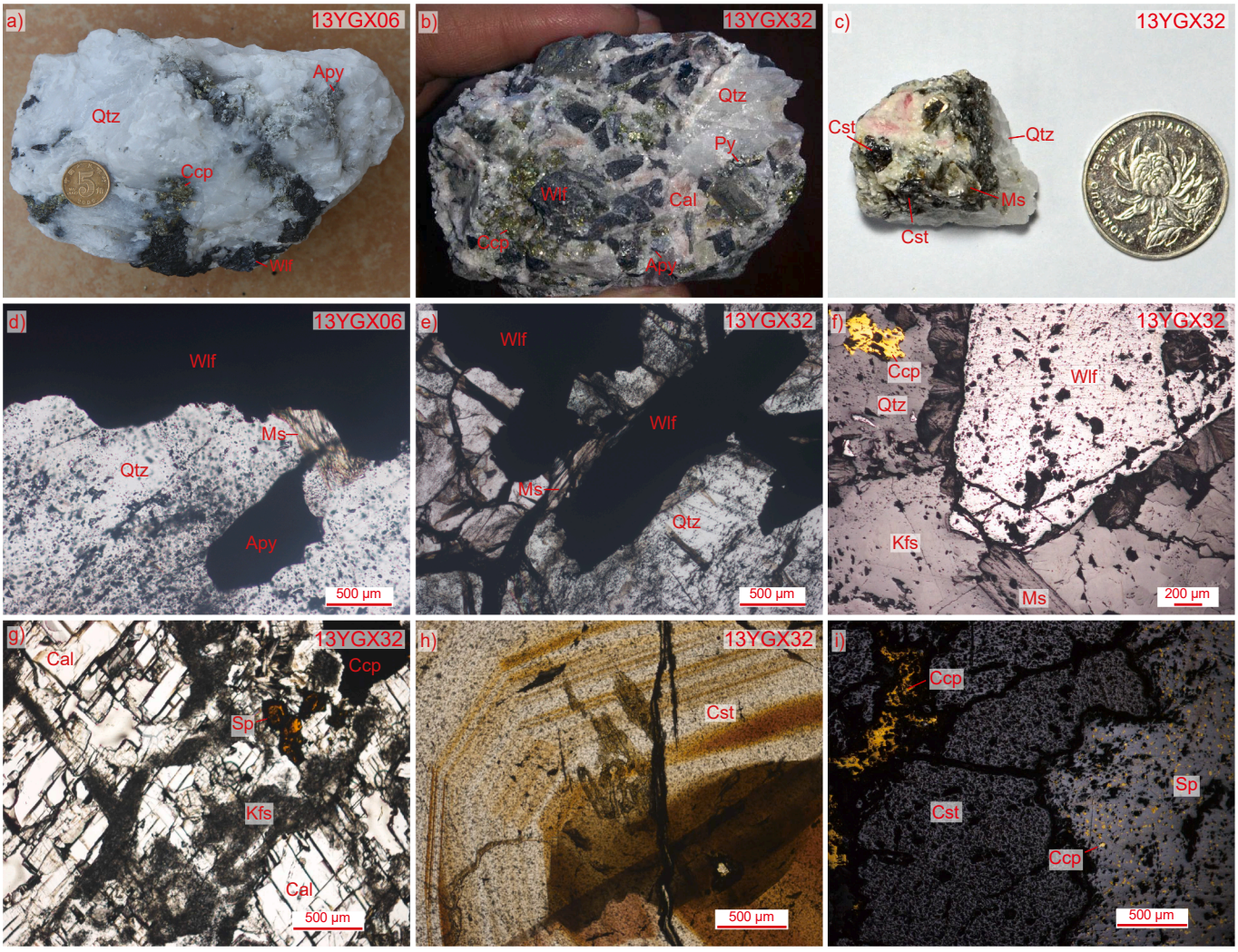

Fig. 2. Representative photographs and photomicrographs of the studied samples. (a–c) Photographs showing intergrowth of quartz, muscovite, sulfides, wolframite and/or cassiterite. (d–g) Photomicrographs showing intergrown wolframite, quartz, muscovite, sulfides and/or calcite. (h) Oscillatory zoning of cassiterite. (i) Chalcopyrite occurs as veins crosscutting cassiterite or as emulsion texture in sphalerite. Micrographs of (f) and (i) were taken using reflected light. Mineral abbreviations: Qtz-quartz, Ccp-chalcopyrite, Apy-arsenopyrite, Wlf-wolframite, Cal-calcite, Py-pyrite, Cst-cassiterite, Ms-muscovite, Kfs-K-feldspar, Sp-sphalerite.

Ramiah, 1959; Lees et al., 1981; Ke, 1998; Frost et al., 2001). Additionally, the Raman peak at 1450 cm^{-1} is ascribed to the CH_2 wagging mode of straight-chain alkanes (e.g., Pironon et al., 1995).

The $A(CO_2/CH_4)$ values of fluid inclusions were calculated as area ratios of the Raman peaks of CO_2 and CH_4 using the software PeakFit (version v.4.12, Singh et al., 2011). The Raman peak area ratio of two gas species allows the calculations of their molar ratio if a quantification factor is given, which is controlled by the Raman scattering cross-section and the spectral efficiency of the microspectrometer (Seitz et al., 1996; Burke, 2001). Without a rigorous calibration process using standards, it is very difficult to obtain the precise quantification factor (Seitz et al., 1996; Blamey, 2012; Frezzotti et al., 2012). The same goes for this study. However, as the studied samples are measured with the same machine under similar experimental conditions, it is reasonable to assume nearly identical quantification factors for all the measured fluid inclusions in the same kind of mineral. The $A(CO_2/CH_4)$ values, therefore, permit the general comparison and discussion of the molar ratios of CO_2 and CH_4 for different types of fluid inclusions in the same mineral. The results are presented in Table A.1 in Appendix A.

3.2. QMS composition analysis

The ore mineral cassiterite and gangue mineral quartz from the two ore-bearing quartz vein samples were selected for gas compositional analysis using an SRS© RGA200® quadrupole mass spectrometer which was coupled with an *in-house* designed stepwise crushing system (Qiu and Wijbrans, 2006; Qiu and Jiang, 2007; Qiu et al., 2011) at the State Key Laboratory of Isotope Geochemistry, Guangzhou Institute of Geochemistry, Chinese Academy of Sciences (GIGCAS). This QMS is equipped with a Faraday cup and an electron multiplier and has a mass range of 1–200 amu (mass to charge ratio), which is sufficient to identify most common gas species. The crushing system consists of a crusher and a Pfeiffer HiCube80 Eco® turbo pumping station that cleans the system immediately after each analysis. The crusher comprises a type 316 L stainless steel tube (length: 160 mm, inner diameter: 28 mm) and a magnetic 3Cr13 type (or S42030) stainless steel pestle. A spherical curvature on the internal base of the crushing tub matches the spherical bottom of the pestle well, which permits more effective crushing of mineral grains. The pestle with a weight of only 214 g was controlled by an external electric magnet. The magnet was controlled by a repeating-timer-relay to repeatedly lift and drop (free-fall) the pestle from a height of 3–5 cm to crush the minerals. These setups permit gentle stepwise crushing with a strength that is more than one-order-of-magnitude lower than those of traditional crushing devices based on the design of Andrawes and Gibson (1979) and Matsumoto et al. (2001). The crushing frequency and drop numbers of each crushing step ("drop" represents the free-fall of the pestle) are adjustable, which allows for rapid extractions of fluid inclusions even when elevated drop numbers were applied and also prevents overburdening of the mass spectrometer.

Prior to crushing, mineral samples with a size range of 380–830 μm were carefully hand-picked under a binocular microscope and rinsed several times with dilute nitric acid followed by deionized water in an ultrasonic bath to remove surface organics. Around 150 mg of dried mineral grains of each sample were loaded at the bottom of the crushing tube together with the pestle. To remove gas impurities absorbed by the surface of the metal tubes, the crushing system, and the connecting tubes were baked at 150 °C for ~20 h using a furnace and heat tapes, respectively.

The experiments were performed at room temperature when high vacuum conditions (4.0×10^{-8} mbar) were achieved inside the machine using a turbo pump. A blank measurement was carried out before each round of sample measurement. During QMS analysis, the gas extraction line was isolated from the mass spectrometer and the vacuum system. The released gases were introduced into the QMS immediately as the crushing steps finished and were analyzed using the Faraday cup of the QMS in static mode. A histogram scan mode was applied to rapidly scan the mass range between 1 and 65 amu, which covers the entire mass range of all the common gases in a magmatic-hydrothermal system. The electron energy and ion energy were set at 70 eV and 12 eV, respectively, for electron impact ionization. When several gas species share overlapping peak patterns, the strongest peaks with the least interferences from other gas fragments were used for quantification purposes. The resulting data were converted to their associated base peaks. After each measurement, the turbo pump was used to clean the entire system. The analytical procedures are similar to those described in Xiao et al. (2019). The results are presented as relative contents in Table A.2 in Appendix A.

3.3. $^{40}Ar/^{39}Ar$ stepwise crushing

The $^{40}Ar/^{39}Ar$ stepwise crushing experiment was performed at Key Laboratory of Tectonics and Petroleum Resources, Ministry of Education, China University of Geosciences (Bai et al., 2018b). The cassiterite sample with grain sizes of 380–830 μm was wrapped in aluminum foil and placed in an aluminum vessel together with biotite monitor standards ZBH-2506 with a $^{40}Ar/^{39}Ar$ plateau age of 132.7 ± 0.1 Ma (1σ, Wang, 1983) which is used for irradiation parameter and *J*-value calculations. ^{39}Ar recoil loss is unavoidable during neutron irradiation but its effect is negligible when the mineral grains are > 100 μm (Paine et al., 2006; Jourdan et al., 2007; Ren and Vasconcelos, 2019). Given that the grain sizes we used are > 380 μm, this effect should be negligible for the studied samples.

The sample was crushed using a similar *in-house* designed stepwise crushing system (Qiu and Wijbrans, 2006; Qiu and Jiang, 2007; Qiu et al., 2011) as the one used for the QMS analysis. The gases released were cleaned using a cryotrap at −110 °C followed by equilibration with a SAES ST101® Zr/Al getter at room temperature and further purification with another Zr/Al getter at 400 °C for 400 s. The purified noble gases were analyzed using an ARGUS VI® mass spectrometer equipped with five Faraday cups and a CDD (compact discrete dynode) ion counting multiplier. The blank measurements were conducted between every three or four rounds of sample measurements.

The *J*-value of the sample was interpolated based on the regression line of *J*-values of co-irradiated monitor standards. $^{40}Ar/^{39}Ar$ data are calculated and plotted using the ArArCALC software (version 2.5.2, Koppers 2002). The total decay constant for ^{40}K used is from Steiger and Jäger (1977): $\lambda = 5.543 \times 10^{-10}$/yr. The correction factors used are $(^{39}Ar/^{37}Ar)_{Ca} = 6.175 \times 10^{-4}$, $(^{36}Ar/^{37}Ar)_{Ca} = 2.348 \times 10^{-4}$ and $(^{40}Ar/^{39}Ar)_{K} = 2.323 \times 10^{-3}$ which were derived from irradiated CaF_2 and K_2SO_4. The results are presented in Table A.3–A.4 in Appendix A.

4. Results

4.1. Fluid inclusion types, petrographic characteristics, and Raman compositions

Fluid inclusions in the studied samples show variable distribution and morphologic features (Figs. 3–5). Based on the discrimination criteria of Roedder (1984) and Goldstein and Reynolds (1994), the fluid inclusions can be grouped into two main generations: primary (PFIs) and secondary (SFIs) fluid inclusions. The PFIs trapped during mineral growth generally occur in three-dimensional clusters or along mineral growth zones. Some of them are randomly distributed between the growth zones. Some small fluid inclusions form linear trends within mineral grains are pseudosecondary fluid inclusions (PSFIs). As the PSFIs also form during the growth of the host minerals and trap similar primary ore-forming fluids as the PFIs, they are not distinguishable from the typical PFIs in the classification and discussion. The SFIs trapped after mineral growth preferentially distribute linearly along micro-cracks. Compared to the PFIs, the SFIs generally have larger sizes and less regular shapes because mineral micro-cracks tend to capture big fluid fluxes during rapid hydrothermal disturbances whereas the PFIs

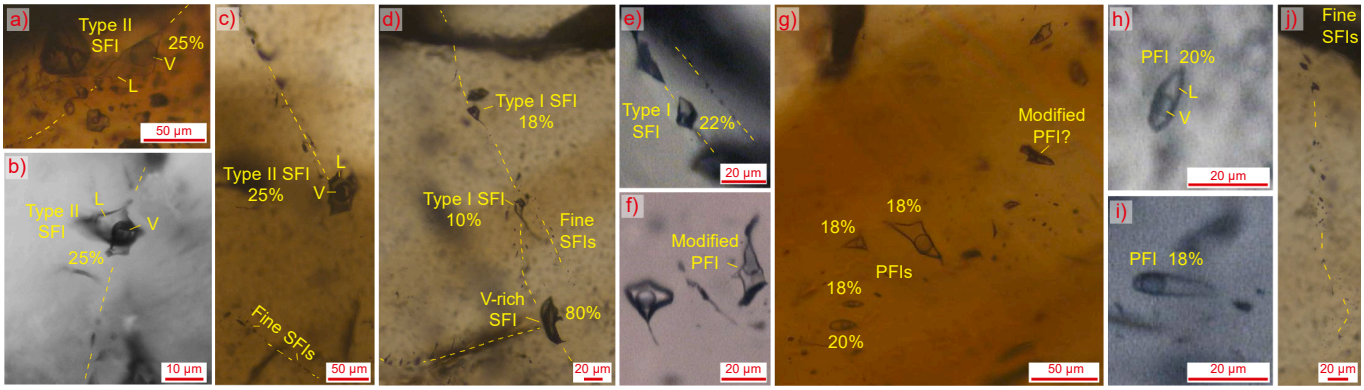

Fig. 3. Representative photomicrographs showing different types of fluid inclusions in the cassiterite sample 13YGX32Cst. (a–e) Secondary fluid inclusions in the cassiterite sample. (f) Modified primary fluid inclusions. (g–i) Linearly distributed and isolated primary fluid inclusions. (j) Linearly distributed very fine secondary fluid inclusions. Micro-cracks of minerals are represented by the dotted lines. Vapor-filling degrees (*f*, expressed as n%) are labeled next to the two-phase fluid inclusions. L, aqueous solution. V, vapor phase. PFI and SFI represent primary and secondary fluid inclusions, respectively.

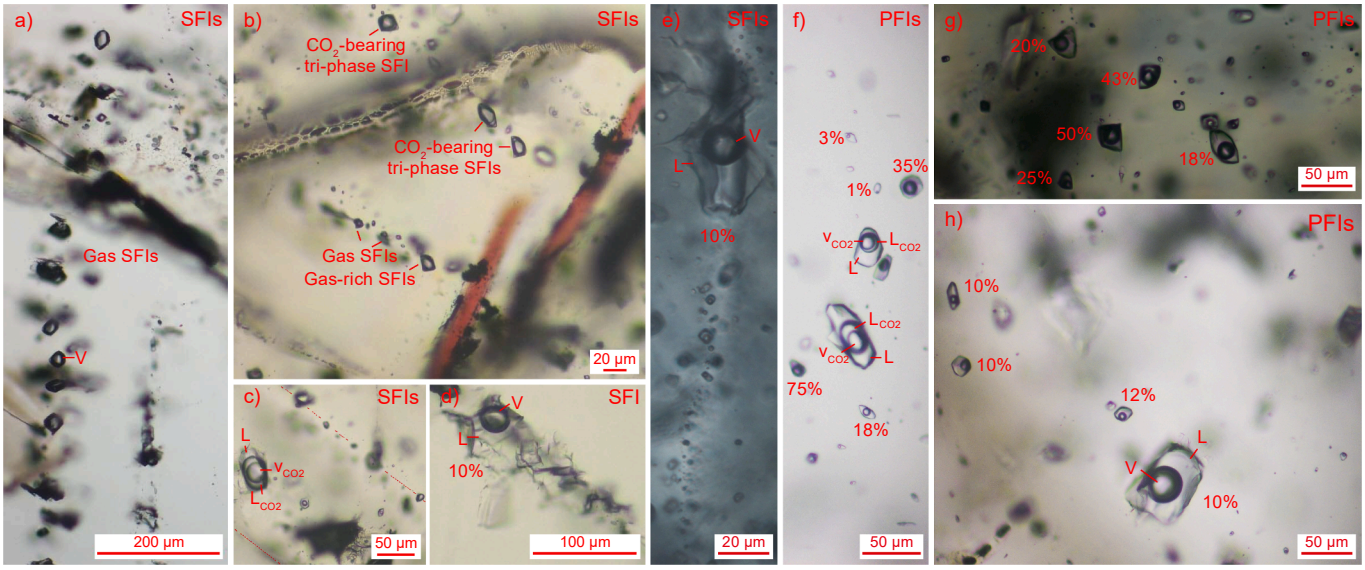

Fig. 4. Representative photomicrographs showing different types of fluid inclusions in the quartz sample 13YGX32Qtz. (a–c) Secondary gas inclusions, gas-rich two-phase, and CO_2-bearing tri-phase fluid inclusions. (d–e) Large liquid-rich secondary fluid inclusions. (f–h) Different types of primary fluid inclusions with distinct sizes and vapor-filling degrees. L_{CO2} and V_{CO2} represent liquid CO_2 and gaseous CO_2, respectively. The expression of mineral micro-cracks, *f*, L, V, PFI, and SFI are the same as those in Fig. 3.

form during the slow growth period of the host mineral in a steady fluid flux, which generally leads to isolated or linear distributions along growth zones/crystal faces with regular shapes. There are also some large and irregular fluid inclusions sporadically distributed in these minerals. Some of them show tiny necks. They are likely modified PFIs because very large fluid inclusions are easily affected by late-stage hydrothermal or structural events which could lead to necking-down, stretching, or non-decrepitative H_2O leakage of the fluid inclusions (e.g., Goldstein and Reynolds, 1994; Audétat and Günther, 1999).

Gas compositions of both the PFIs and the SFIs within the studied minerals were analyzed using Raman spectroscopy. The calculated Raman $A(CO_2/CH_4)$ values of different types of fluid inclusions are presented in Fig. 6. When microscopic observations (see Figs. 3–5) are combined with Raman analysis (see Fig. 6), PFIs and SFIs in the studied samples can be further subdivided into several different types. Their relative proportions in the minerals are estimated and presented in Table 1 and their physical and chemical characteristics are described in the following text.

4.1.1. *Fluid inclusions in cassiterite sample 13YGX32Cst*

Fluid inclusions in the cassiterite sample 13YGX32Cst are mainly liquid-rich two-phase with minor gas-rich two-phase and gas inclusions (Fig. 3). CO_2-bearing tri-phase fluid inclusions are absent (Fig. 3). The SFIs are mainly liquid-rich and two-phase. They generally display irregularly elongated shapes along mineral boundaries or mineral micro-cracks (Fig. 3a–e). Two types of liquid-rich two-phase SFIs, i.e., Type I and Type II SFIs, can be identified based on their sizes, vapor-filling degrees (expressed as *f*, represents the volume percentage of the vapor), and their Raman compositions. Type I SFIs, accounting for ~15% of the bulk fluid inclusions, have smaller sizes, lower *f* values (e.g., Fig. 3d and e), and very low $A(CO_2/CH_4)$ values ($\ll 1$, Fig. 6a). Type II SFIs, accounting for ~25% of the bulk fluid inclusions, are relatively larger (some can be up to 110 μm, e.g., Fig. 3a–c) and usually have extremely irregular shapes, slightly higher but more variable *f* values, and much higher $A(CO_2/CH_4)$ values (> 1) (Fig. 6a) than Type I SFIs. PFIs in the sample are mainly liquid-rich two-phase with relatively regular shapes (Fig. 3g–i). They are generally isolated while some are distributed linearly along mineral growth zones (Fig. 3g). These PFIs are methanoic with significant CH_4 but negligible CO_2 Raman signatures,

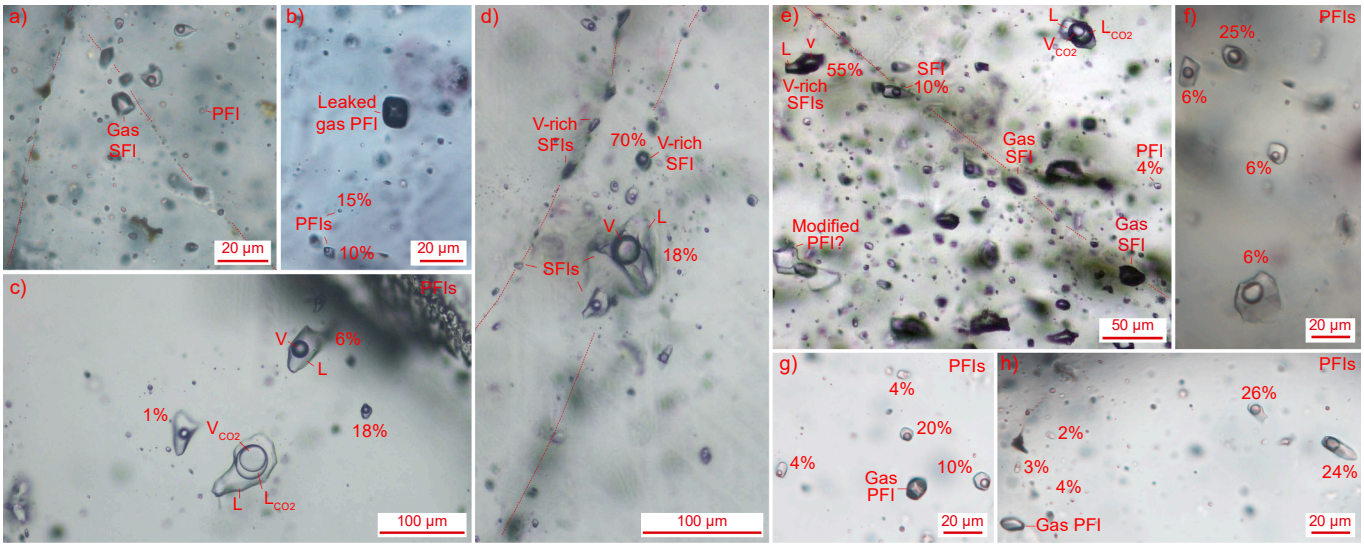

Fig. 5. Representative photomicrographs showing different types of fluid inclusions in the quartz sample 13YGX06Qtz. (a–b) Secondary and leaked gas inclusions. (c) CO_2-bearing tri-phase fluid inclusions coexisting with large liquid-rich primary fluid inclusions. (d) Large liquid-rich secondary fluid inclusions. (e) Coexistence of multiple types of fluid inclusions. (f–h) Primary fluid inclusions with distinct sizes and vapor-filling degrees. The expression of mineral micro-cracks, *f*, L, V, L_{CO2}, V_{CO2}, PFI, and SFI are the same as those in Fig. 3 and 4.

which correspond to very low $A(CO_2/CH_4)$ values ($\ll$ 1, Fig. 6a). Modified PFIs are sporadically distributed in the cassiterite sample. They generally have large sizes, extremely irregular shapes (e.g., Fig. 3f), and are also methanoic in composition (Table A.1). Additionally, very fine beak-like or linearly distributed SFIs also developed in the sample and their abundance is different from grain to grain (Fig. 3d, g and j). Their gas compositions are currently undetermined due to their very small sizes (less than several micrometers).

4.1.2. Fluid inclusions in quartz sample 13YGX32Qtz

Fluid inclusions in quartz sample 13YGX32Qtz have more complicated features compared to its spatially associated cassiterite sample 13YGX32Cst cited above. Fluid inclusions in this sample show the following characteristics (see Fig. 4): 1) abundant secondary gas inclusions, gas-rich two-phase SFIs, and CO_2-bearing tri-phase SFIs distribute along micro-cracks (Fig. 4a–c), which are CO_2-rich with $A(CO_2/CH_4)$ values > 1 (Fig. 6b); 2) very large (usually > 50 μm) liquid-rich SFIs are widespread (Fig. 4d and e), which are also CO_2-rich with high $A(CO_2/CH_4)$ values (> 1, Fig. 6b), and 3) PFIs ranging from tens of micrometers to nanoscale (mostly are 20–50 μm) with distinct vapor-filling degrees (Fig. 4f–h) are generally considered as products of fluid immiscibility. These PFIs are mainly CO_2-rich in composition with high $A(CO_2/CH_4)$ values (> 1, Fig. 6b) except for minor smaller ones (generally < 10 μm, f < 12%) that have $A(CO_2/CH_4)$ values < 1 (Fig. 6b).

4.1.3. Fluid inclusions in quartz sample 13YGX06Qtz

Quartz sample 13YGX06Qtz is characterized by multiple types of fluid inclusions in terms of their sizes, phases, and vapor-filling degrees (Fig. 5). Pure gas SFIs are usually distributed along micro-cracks (Fig. 5a and e). There is a group of isolated inclusions with regular shapes similar to pure gas PFIs but with dark black surfaces (e.g., Fig. 5b). Raman experiments failed to detect any gas species in them, which indicates that the gases might have leaked during late-stage events. Tri-phase CO_2-bearing PFIs and SFIs are widely distributed in the sample (Fig. 5c and e). They generally have very large sizes (up to 100 μm) and very high $A(CO_2/CH_4)$ values (2.34–14.50, Table A.1). Additionally, abundant very large liquid-rich two-phase SFIs (20–80 μm) and minor gas-rich two-phase SFIs are present (Fig. 5d and e). These SFIs have relatively irregular shapes and are characterized by high $A(CO_2/CH_4)$ values (> 1, Fig. 6b). In addition to the CO_2-bearing tri-phase PFIs cited above, liquid-rich two-phase PFIs also widely exist and can be divided into three subgroups: i.e., 1) dominated medium-sized CO_2-rich ($A(CO_2/CH_4)$ > 1, Fig. 6b) PFIs with higher f values (15–30 μm, f = 10–30%, Fig. 5f and h), 2) subordinate large CO_2-rich ($A(CO_2/CH_4)$ > 1) PFIs with low f values (20–60 μm, f < 10%, Fig. 5c and f), and 3) minor small methanoic ($A(CO_2/CH_4)$ < 1, Fig. 6b) PFIs with low f values (usually less than several micrometers, f < 10%, Fig. 5f–h). The higher-f PFIs generally show round or elongated shapes whereas those with lower f values have sharp edges (Fig. 5c and f–h).

4.2. QMS gas composition analysis

QMS gas composition analysis was conducted on the cassiterite and quartz samples. The results are listed in Table A.2 and presented in Figs. 7–9. The dominant gas components of the fluid inclusions in the studied minerals are CO_2, CH_4, N_2, H_2O, and organic species that mainly include formamide (amu = 45), ethane, propane, and butane. He, Ar, and O_2 also occur as minor components in fluid inclusions. In the following sections, the chemical characteristics of the major gas components are discussed.

During the crushing process, gas compositions vary from one crushing step to another. Based on the variations of the CO_2/CH_4 ratios and the relative contents of the major gas components, the whole crushing process could be broadly divided into three crushing stages: the initial, intermediate, and final crushing stages (see Figs. 7–9 and Table A.2). Gases released in the initial crushing stage (usually less than tens to hundreds of drops of crushing) generally show high CO_2, C_4H_{10}, and low H_2O contents and elevated CO_2/CH_4 ratios (> 1). Gases liberated in the intermediate crushing stage usually show gradually enhanced proportions of H_2O and formamide (some of them even reach the peak values in this stage). Gases extracted from the final crushing stage (usually up to thousands of drops of crushing) have extremely high CH_4 and C_3H_8 contents but very low CO_2/CH_4 ratios (< 1).

Notably, the crushing experiment of the quartz sample 13YGX32Qtz showed more complicated features in the initial crushing stage. As shown in Fig. 8a, steps 1–17 (19 drops in total) in the initial crushing stage have almost uniform and slightly elevated CO_2/CH_4 ratios (1.51–1.90) whereas the subsequent steps 18–46 (102 drops in total) have disordered and elevated CO_2/CH_4 ratios (1.85–2.94).

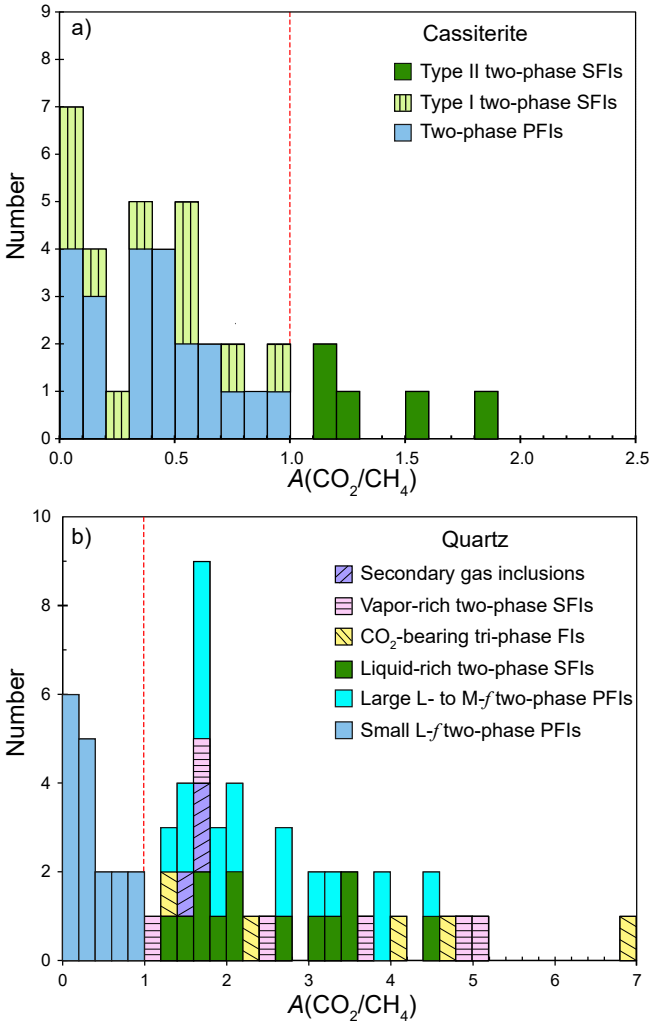

Fig. 6. Histogram of calculated Raman $A(CO_2/CH_4)$ values of different types of fluid inclusions within cassiterite and quartz samples. The relative peak areas of CO_2 and CH_4 (expressed as $A(CO_2/CH_4)$) were calculated by area ratios of Raman peaks for CO_2 and CH_4. Data are from Xiao et al. (2019) and this study (see Table A.1 in Appendix A).

4.3. $^{40}Ar/^{39}Ar$ stepwise crushing of the cassiterite sample

The irradiated counterpart of the ore mineral cassiterite sample 13YGX32Cst was selected for $^{40}Ar/^{39}Ar$ stepwise crushing. The results are presented in Tables A.3–A.4 (also see Fig. 10). The $^{40}Ar/^{39}Ar$ stepwise crushing experiment of the cassiterite sample 13YGX32Cst yielded a steadily decreasing age spectrum for the first 4 crushing steps (290 drops of crushing) with anomalously old apparent ages and an upward-convex age spectrum for the final crushing steps. The inverse isochron of steps 5–14 (4690 drops of crushing) has an initial $^{40}Ar/^{36}Ar$ ratio of 302.0 ± 1.0, which is higher than the atmospheric ratio of 295.5 (Steiger and Jäger, 1977), indicating excess argon. Excluding excess ^{40}Ar by assuming the initial $^{40}Ar/^{39}Ar$ value of 302.0 yields a flat age spectrum of these steps with a plateau age of 152.9 ± 3.2 Ma (MSWD = 0.1), which is consistent with the isochron age of 152.9 ± 6.0 Ma (MSWD = 0.1) for this sample.

Gases released during the first 4 crushing steps of this sample exhibited good linear correlations on plots of $^{38}Ar_{Cl}$–$^{39}Ar_K$–$^{40}Ar^*$ correlation diagrams (Fig. 10c–d). Ages calculated from the slope and the X-intercept are 129.2 ± 13.9 Ma and 129.3 ± 13.9 Ma, respectively. As the crushing experiment proceeds, the $^{40}Ar^*/^{39}Ar_K$ ratios dropped to relatively uniform levels and formed a good linear correlation on the plot of $^{40}Ar^*/^{38}Ar_{Cl}$ versus $^{39}Ar_K/^{38}Ar_{Cl}$ (Fig. 10c–d). The ages calculated from the $^{40}Ar^*/^{39}Ar_K$ ratios on the plot of $^{38}Ar_{Cl}/^{40}Ar^*$ versus $^{39}Ar_K/^{40}Ar^*$ have an average age of 152.7 ± 2.3 Ma and the age calculated from the slope of the regression line on the plot of $^{40}Ar^*/^{38}Ar_{Cl}$ versus $^{39}Ar_K/^{38}Ar_{Cl}$ is 153.1 ± 2.3 Ma. These ages agree well with their plateau and isochron ages.

5. Discussion

5.1. A general model of gas release patterns of fluid inclusions during stepwise crushing

5.1.1. Low-density gas-rich fluid inclusions

As shown in the crushing experiments above (see Figs. 7–9), the very low proportions of H_2O in the initial crushing stage suggest that gas-rich sources such as gases captured in mineral micro-cracks, gas inclusions, and gas-rich fluid inclusions dominate the degassing budget. Notably, the gases released from initial crushing steps (steps 1–17) of the sample 13YGX32Qtz have uniform and slightly elevated CO_2/CH_4 ratios (1.51–1.90, Fig. 8a) which resemble those from secondary gas inclusions and gas-rich SFIs along micro-crocks (Fig. 8c and d). It is worth noting that extraordinarily large amounts of CO_2-rich and H_2O-poor gases are released during the first tens of crushing steps of this sample (Table A.2), which likely originate from gas inclusions that are widespread along the micro-cracks (Fig. 4a). In contrast, gases released in the following dozens of crushing steps 18–46 of this sample are still H_2O-poor and CO_2-rich but show higher CO_2/CH_4 ratios (1.85–2.94, Fig. 8a). This indicates the evacuation of CO_2-rich gas-rich sources, especially, the CO_2-bearing tri-phase fluid inclusions (both PFIs and SFIs) because these inclusions generally have low H_2O contents but higher Raman $A(CO_2/CH_4)$ ratios relative to other fluid inclusions (e.g., Fig. 8e, also see Fig. 6b). Taken together, fluid inclusions with high vapor-filling degrees, specifically, pure gas inclusions distributed along micro-cracks that were only filled with low-density gases, are most likely extracted at the very initial stage of crushing (Fig. 11a). Meanwhile, fluid inclusions that contain high CO_2 contents in the vapor are also the more easily extracted group due to their higher internal pressures.

On the other hand, super-large fluid inclusions, regardless of whether they are secondary (very common in the mineral) or primary (if any) fluid inclusions, are likely also preferentially broken during initial crushing steps. This is supported by the degassing pattern of the cassiterite sample (Fig. 7b) where high proportions of formamide from the initial crushing stage correspond to the breakup of Type II SFIs (e.g., Fig. 7c and d) with sizes up to 100 μm.

5.1.2. Large liquid-rich fluid inclusions

Gases extracted in the intermediate crushing stage have CO_2/CH_4 ratios that vary from high (> 1) to low values (< 1) (see Figs. 7–9). Some even display a linear relationship marked by continually decreasing CO_2/CH_4 ratios (e.g., sample 13YGX32Qtz, Fig. 8a). This likely indicates that the extracted gases during the intermediate crushing stage represent a mixture of both SFIs and PFIs, which successively evolved from SFIs- to PFIs-dominated regimes. It is worth noting that the H_2O contents in this crushing stage increased gradually, which suggests a gradual transition of the degassing sources from gas-rich to liquid-rich sources. Additionally, the peak values of the formamide contents in this crushing stage (Figs. 8–9) indicate a formamide-rich source. We propose that gases extracted in this stage are mainly from large liquid-rich and CO_2-rich SFIs, as well as some large liquid-rich PFIs (usually modified by late-stage events) with relatively high f values as both of them contain considerable amounts of H_2O and formamide (Fig. 8f and g and Fig. 9e, f and g). In contrast, the small methanoic PFIs were most likely unaffected since they have the lowest Raman $A(CO_2/CH_4)$ ratios while gases released in these steps have high CO_2/CH_4 ratios (> 1) (Figs. 7–9).

Compared with the two quartz samples studied above, the cassiterite sample 13YGX32Cst showed different gas release patterns in the

Table 1
Major fluid inclusion types and their proportions in hydrothermal minerals from the Yaogangxian tungsten deposit, South China.

Samples	Generation	PFIs			Modified PFIs		SFIs			Fine SFIs
	composition	(aquo) CH_4-rich	(aquo) CO_2-rich		(aquo) CH_4-rich	(aquo) CO_2-rich	(aquo) CH_4-rich	(aquo) CO_2-rich		Unknown
	phase correlations	two-phase	two-phase	single-, two- or tri-phases	generally two-phase	single-, two- or tri-phases	two-phase	two-phase	single-, two- or tri-phases	single-, two- or tri-phases
		L-rich, low-*f*	L-rich, relatively high-*f*	V-rich, high-*f*	L- to V-rich, relatively high-*f*	L- to V-rich, relatively high-*f*	L-rich, low-*f*	L-rich, low-*f*	V-rich, high-*f*	L- to V-rich, low- to high-*f*
Quartz vein sample 13YGX32 with a mineral association of quartz, muscovite, wolframite, arsenopyrite, chalcopyrite, fluorite, K-feldspar, calcite, and cassiterite.										
13YGX32Cst	proportion	~ 46%	–	–	~ 8%	–	~15%	~25%	< 1%	< 5%
	diameter	< 40 μm	–	–	> 20 μm	–	20–50 μm	20–110 μm	~ 25 μm	< 5 μm
13YGX32Qtz	proportion	< 10%	~ 20%	~10%	–	~ 5%	–	~ 35%	~ 17%	< 3%
	diameter	< 10 μm	15–30 μm	20–50 μm	–	> 20 μm	–	20–80 μm	10–30 μm	< 5 μm
Quartz vein sample 13YGX06 with a mineral association of quartz, muscovite, wolframite, arsenopyrite, chalcopyrite, pyrite, and cassiterite.										
13YGX06Qtz	proportion	< 10%	~ 20%	~20%	–	~ 6%	–	~30%	~ 12%	< 2%
	diameter	< 10 μm	15–30 μm	20–100 μm	–	> 15 μm	–	20–80 μm	20–50 μm	< 5 μm

Note: Proportions of different types of fluid inclusions were visually estimated. The symbol "–" denotes insignificant amounts or absence. Abbreviations: PFIs–primary fluid inclusions, SFI–secondary fluid inclusions, aquo–aqueous, L–liquid, V–vapor, *f*–vapor-filling degree of a fluid inclusion (expressed as n%). The composition classification of the fluid inclusions is mainly based on the Raman $A(CO_2/CH_4)$ values that those with Raman $A(CO_2/CH_4)$ values > 1 are CO_2-rich whereas those with Raman $A(CO_2/CH_4)$ values < 1 are methanoic.

intermediate crushing stage (Fig. 7a–b), which should be related to the distinct fluid inclusion characteristics in the cassiterite. For example, the formamide and CO_2 proportions of the cassiterite sample vary dramatically, which is accompanied by rapidly decreasing CO_2/CH_4 ratios in this stage. This likely resulted from mixing between gases from the CO_2-rich and formamide-bearing Type II SFIs (Fig. 7c and d) and gases from the CH_4-rich and formamide-poor Type I SFIs (Fig. 7e).

5.1.3. Small fluid inclusions

Gases released in the final crushing stage (usually after thousands of pestle drops) generally show intermediate to high H_2O contents (Figs. 7–9) indicating aqueous fluid inclusion sources. The variable compositions of H_2O, C_2H_6, formamide, and N_2 in these crushing stages of the three studied samples also suggest that contribution from the crusher is insignificant. Typically, these gases are characterized by relatively high CH_4 and low CO_2 contents with very low CO_2/CH_4 ratios ($\ll 1$), which indicate methanoic sources, namely the small methanoic PFIs, with negligible contamination of gases from the CO_2-rich sources. For the cassiterite sample 13YGX32Cst, even though methanoic Type I SFIs are also present, their spatial distribution along micro-cracks would lead to their preferential breakup by stress relative to the isolated PFIs (Fig. 11b). Additionally, the peak values of the N_2 contents in steps 10–14 and the significant elevation of the CH_4 and H_2O proportions from the subsequent steps 15–21 in the final crushing stage (Fig. 7b) indicate successive releases of the larger PFIs (usually modified) with higher *f* values, which show an apparent Raman signature of N_2 (e.g., Fig. 7f), and smaller PFIs, which are typically aqueous methanoic (Fig. 7g and h).

It is noteworthy that multiple types of PFIs with distinct phase behaviors and compositions coexist in the studied quartz samples. For example, high-*f* PFIs and some low-*f* large PFIs are CO_2-rich with high Raman $A(CO_2/CH_4)$ ratios > 1 (Fig. 6b) whereas the low-*f* smaller ones are methanoic with $A(CO_2/CH_4)$ ratios $\ll 1$, which is likely a result of fluid immiscibility. The fact that only methanoic gases are released in the final crushing stage suggests that the CO_2-rich PFIs, including PFIs with high *f* values (either large or small) and some large PFIs, are extracted during earlier crushing steps such as the intermediate crushing stage (Fig. 11b), whereas the methanoic PFIs, which are small with lower *f* values, are extracted later, especially, in the final crushing stage (Fig. 11c). In addition to the vapor-filling degrees and sizes of the fluid inclusions, the relatively higher inner pressures of the CO_2-rich PFIs may also contribute to their earlier extraction than the CH_4- and H_2O-rich PFIs.

The gases released in the last several crushing steps of the cassiterite sample also show a simultaneous C_2H_6 peak (Fig. 7b), which most likely resulted from the degassing of very fine SFIs that are very common in this cassiterite (Fig. 3g). This agrees with the proposed gas release pattern of Xiao et al. (2019) where very fine SFIs (if any) were released when sufficient numbers of crushing were applied. This hypothesis is also supported by increasing amounts of SFI-associated gases such as CO_2, formamide, and C_2H_6 together with $^{38}Ar_{Cl}$ in final crushing steps of the cassiterite sample from Xiao et al. (2019). Recent stepwise crushing experiments on quartz samples from Xiao et al. (2021) also showed elevated proportions of large molecules such as C_3H_8, C_2H_6, N_2, and/or CH_4 after 9000 drops of crushing, which further demonstrates that fluid inclusions, rather than solid phases such as mineral lattices and impurities, are the predominant gas source during prolonged crushing. It is hard to evaluate the contribution of these tiny fluid inclusions during analysis as we were unable to reveal their chemical compositions by traditional analytical methods such as Raman spectroscopy. However, significant release of these tiny fluid inclusions could cause considerable interference for the analytical results of the PFIs, for example, by introducing higher $^{40}Ar^*$ contents and thus older $^{40}Ar/^{39}Ar$ apparent ages in final crushing steps (Xiao et al., 2019).

5.1.4. Overview of the general model of gas release patterns

Overall, the vapor-filling degree (*f* value), inclusion size, composition, and spatial distribution of fluid inclusions in hydrothermal minerals are important factors that control their degassing sequences during gentle stepwise crushing experiments. Building upon the results of Xiao et al. (2019) (see Fig. 12a), the effort of this study allows us to propose a more detailed model of gas release patterns of fluid inclusions for

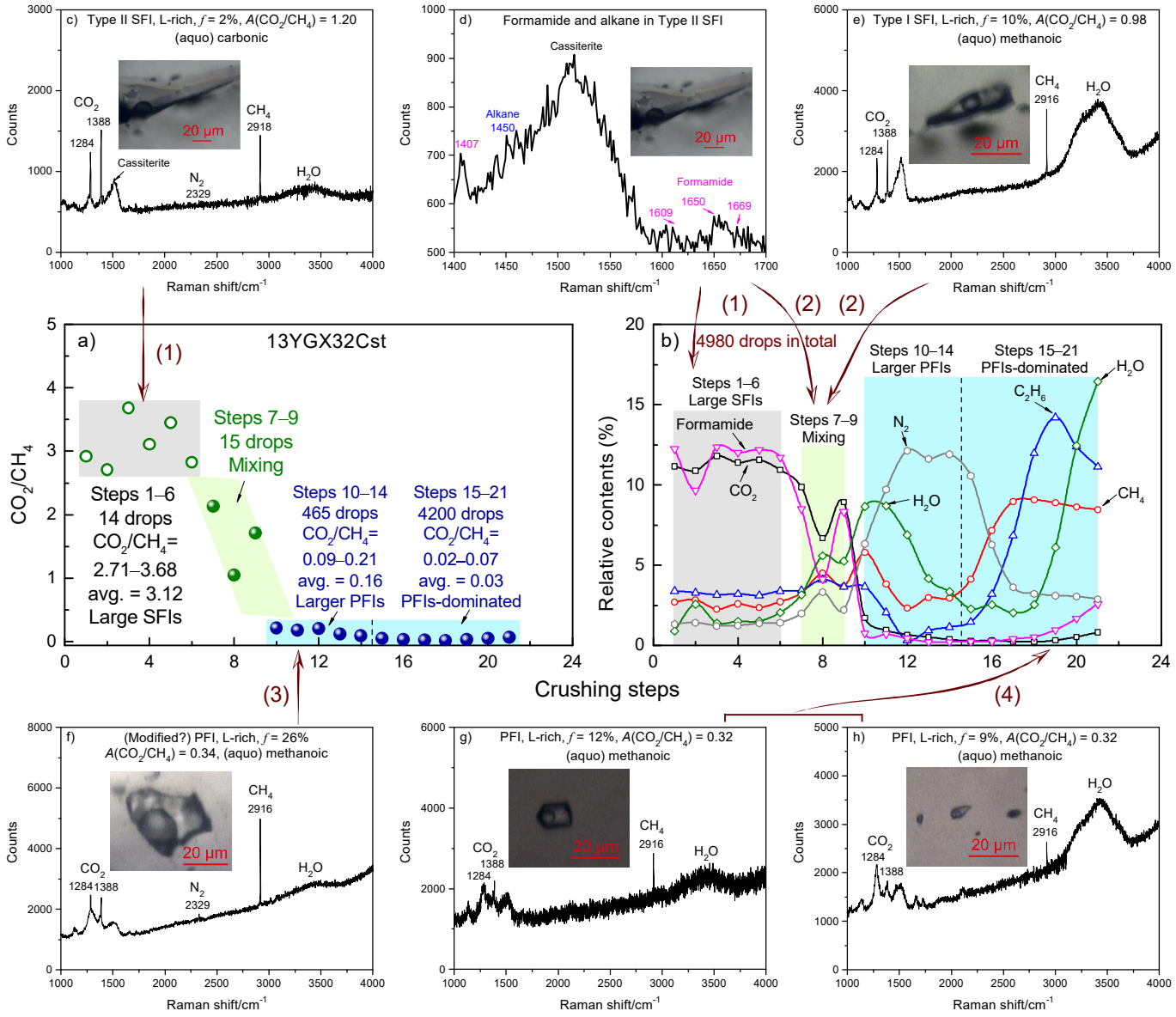

Fig. 7. Results of combined analyses of Raman and QMS gas composition of the cassiterite sample 13YGX32Cst. The light grey, green, and blue shadows represent the initial, intermediate, and final crushing stages, respectively. "Drops" represent the free-fall numbers of the pastel during crushing. The pestle drop numbers and potential gas sources of each crushing stage are also shown. The relative proportion (*r*) in figure (b) represents the content of each crushing step (C_i) accounts for the proportion of the total contents of all the crushing steps ($\sum_{i=1}^{n} C_i$) of gas i, for example, $r = C_i / \sum_{i=1}^{n} C_i$. Vapor-filling degrees (*f*) of the two-phase fluid inclusions analyzed are presented in the Raman spectra. The $A(CO_2/CH_4)$ ratio can roughly represent molar proportions of CO_2 and CH_4, which was calculated as area ratios of the Raman peaks of CO_2 and CH_4 using the software PeakFit (version v.4.12, Singh et al., 2011). V-rich and L-rich represent gas-rich and liquid-rich, respectively. (For interpretation of the references to colour in this figure legend, the reader is referred to the web version of this article.)

hydrothermal minerals during *in-vacuo* gentle stepwise crushing (Fig. 12b). In this model, we propose that large fluid inclusions with high vapor-filling degrees and inner pressures, specifically, pure gas SFIs are preferentially extracted in the initial crushing stage. Soon after, large liquid-rich fluid inclusions, both SFIs and PFIs, are released during the intermediate crushing stage to generate gas mixtures with variation trends from SFIs- to PFIs-dominated origins. During the final crushing stage, the small liquid-rich PFIs with very low vapor-filling degrees are extracted. This is compatible with the observation that the SFIs generally form along micro-cracks and have larger sizes and irregular shapes relative to the small PFIs (Figs. 3–5). Very fine fluid inclusions, usually the SFIs (if any), can also be extracted in the final crushing steps together with the PFIs. The model presented here provides a theoretical basis to understand how different generations of fluid inclusions could be successively extracted through gentle stepwise crushing.

5.2. Application of the general model of gas release patterns

The general model built by this study applies to most terrestrial hydrothermal systems, especially high-temperature magmatic-hydrothermal systems. In most magmatic-hydrothermal or hydrothermal systems, the growing crystals entrap tiny crystal cavities with hydrothermal fluids to form PFIs at a fluid-sufficient, slow, and stable environment and the generated PFIs are usually very small and regular. After mineral growth, multiple episodes of hydrothermal perturbations may affect the systems to varying degrees and the resultant hydrothermal fluids with different sources may be captured by mineral micro-fractures to form multiple generations, types, and phases of SFIs. These SFIs,

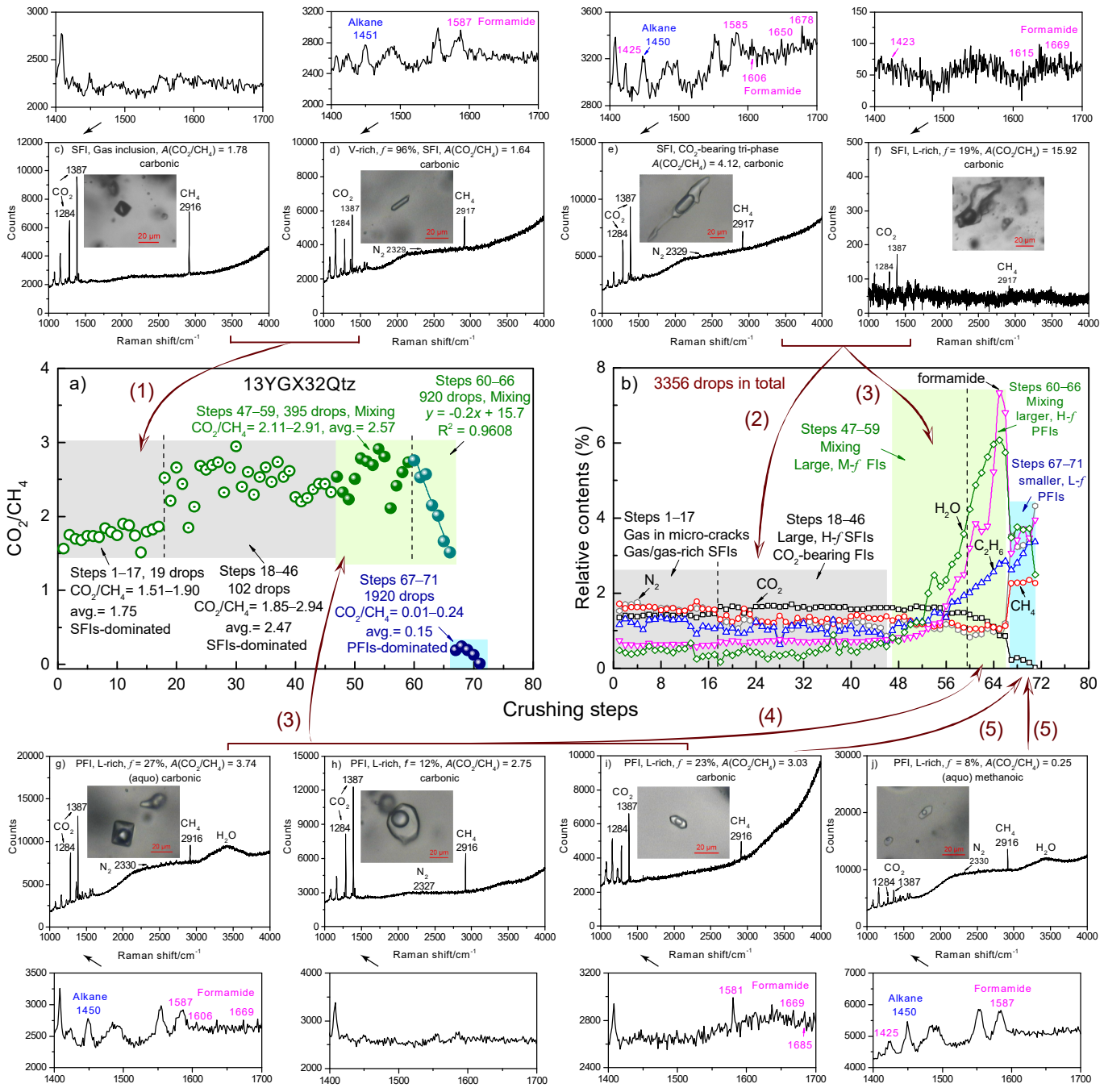

Fig. 8. Results of combined analyses of Raman and QMS gas composition of the quartz sample 13YGX32Qtz. The calculations of relative proportions (r), vapor-filling degrees (f), and $A(CO_2/CH_4)$ ratios are the same as those in Fig. 7.

especially the large ones (either gas-rich or liquid-rich), usually occupy a significant proportion of the mineral-hosted fluid inclusions. Their presence may be the biggest obstacle for accurate isotope and composition analyses of primary fluids (Villa, 2001; Qiu et al., 2002). On the basis of this proposed gas release model, the gentle stepwise crushing technique permits us to effectively distinguish the PFI gases from the SFI gases because these SFIs generally formed at less stable environments with larger sizes, less regular shapes, and fissure-controlled distributions which would lead to their preferential degassing relative to the small PFIs during gentle stepwise crushing.

Hydrothermal minerals could also undergo complex fluid processes such as fluid immiscibility or boiling during evolution, this general model also allows us to identify the source of the extracted gases during gentle stepwise crushing. For example, fluid inclusions that are rich in low-density gases would be extracted earlier than the liquid-rich ones when they have similar sizes and distributions.

Additional experiments may be necessary to further constrain the degassing behaviors in metamorphic and sedimentary minerals with different fluid trapping behaviors. However, this gas release model is still of reference significance as it summarizes the degassing behaviors of multiple types and phases of fluid inclusions. In short, large, irregular, or gas-rich fluid inclusions, especially those distributed along micro-cracks, will always be the most easily extracted groups during gentle stepwise crushing. We now summarize the implications of this general model of gas release patterns for progressive geochronological and compositional analyses in the following text.

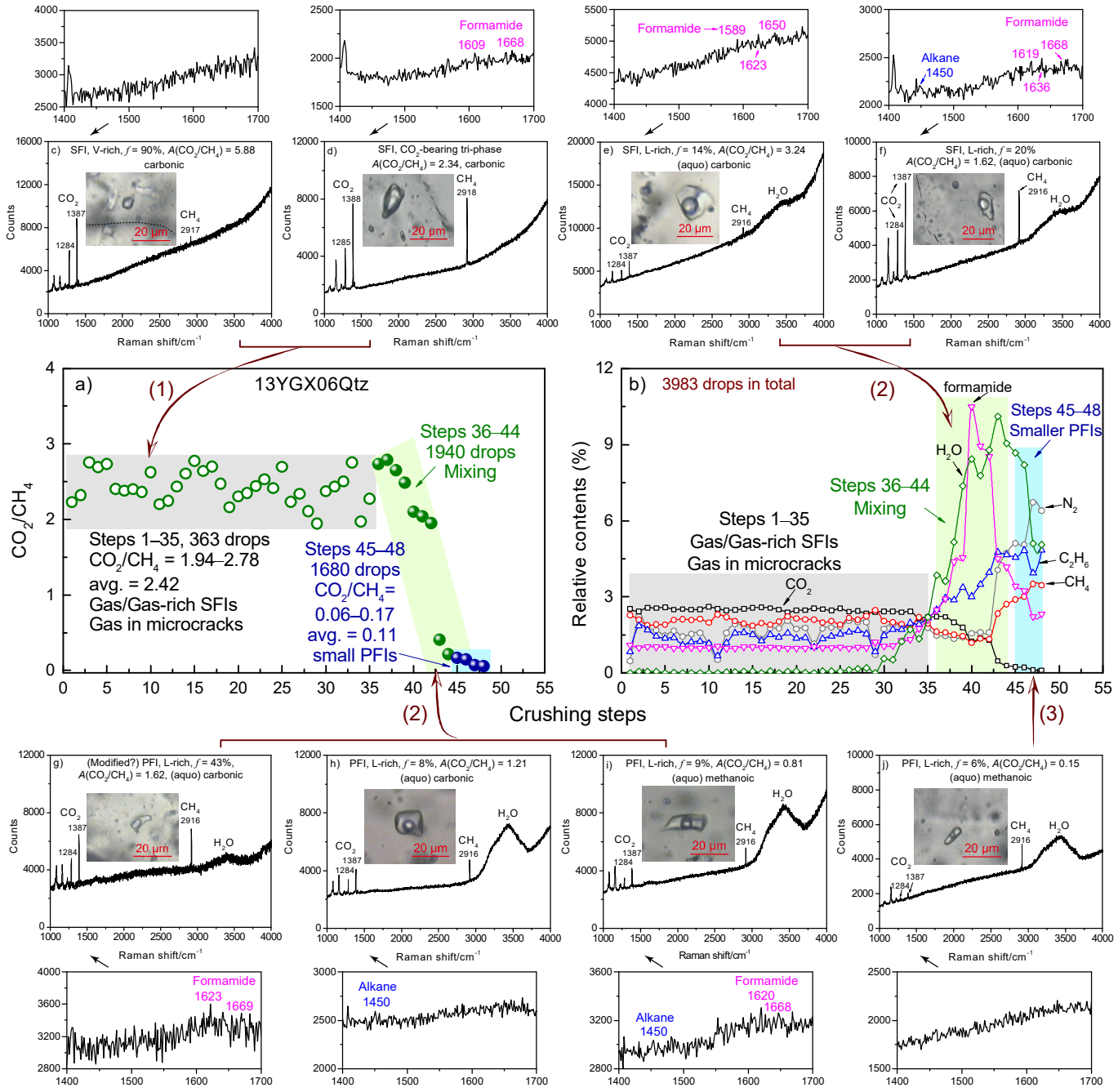

Fig. 9. Results of combined analyses of Raman and QMS gas composition of the quartz sample 13YGX06Qtz. The calculations of relative proportions (*r*), vapor-filling degrees (*f*), and $A(CO_2/CH_4)$ ratios are the same as those in Fig. 7.

5.2.1. Implication for dating different generations of fluid inclusions

It is very difficult to directly date hydrothermal activities via fluid inclusions since most hydrothermal minerals commonly host multi-phases/generations of fluid inclusions. While the stepwise crushing technique has the potential to extract different generations of fluid inclusions and to date them properly (e.g., Qiu et al., 2002; Qiu and Wijbrans, 2006; Bai et al., 2013; Shi et al., 2018; Xiao et al., 2019), our knowledge regarding the degassing process during crushing is still fragmental.

The current study demonstrates that SFIs and/or gas inclusions can be preferentially extracted by initial stepwise crushing steps while the PFI gases are primarily released in the final crushing stage. This view is supported by the $^{40}Ar/^{39}Ar$ dating experiment of cassiterite sample 13YGX32Cst. By preferentially excluding the gas interferences from most Type I and II SFIs, the $^{40}Ar/^{39}Ar$ age of the PFIs (around 153 Ma) was obtained in the final crushing steps (Fig. 10). This age is close to the ore-forming timing (163–153 Ma) of the deposit obtained by different methods including Re–Os dating of molybdenite (Peng et al., 2006; Wang et al., 2010), $^{40}Ar/^{39}Ar$ stepwise heating of phlogopite and muscovite (Peng et al., 2006; Xiao et al., 2019), fluid inclusion $^{40}Ar/^{39}Ar$ stepwise crushing of wolframite, cassiterite and quartz samples (Xiao et al., 2019) as well as *in-situ* LA-ICP MS U–Pb dating of wolframite and cassiterite (Deng et al., 2019; Li et al., 2020).

The general model of gas release patterns proposed here suggests that it is possible to date the SFIs if a certain group of the SFIs dominates the extracted gases during crushing, usually from the earlier crushing stages. The $^{40}Ar/^{39}Ar$ age of the post-mineralization hydrothermal event recorded by the SFIs is, therefore, obtainable. During stepwise crushing

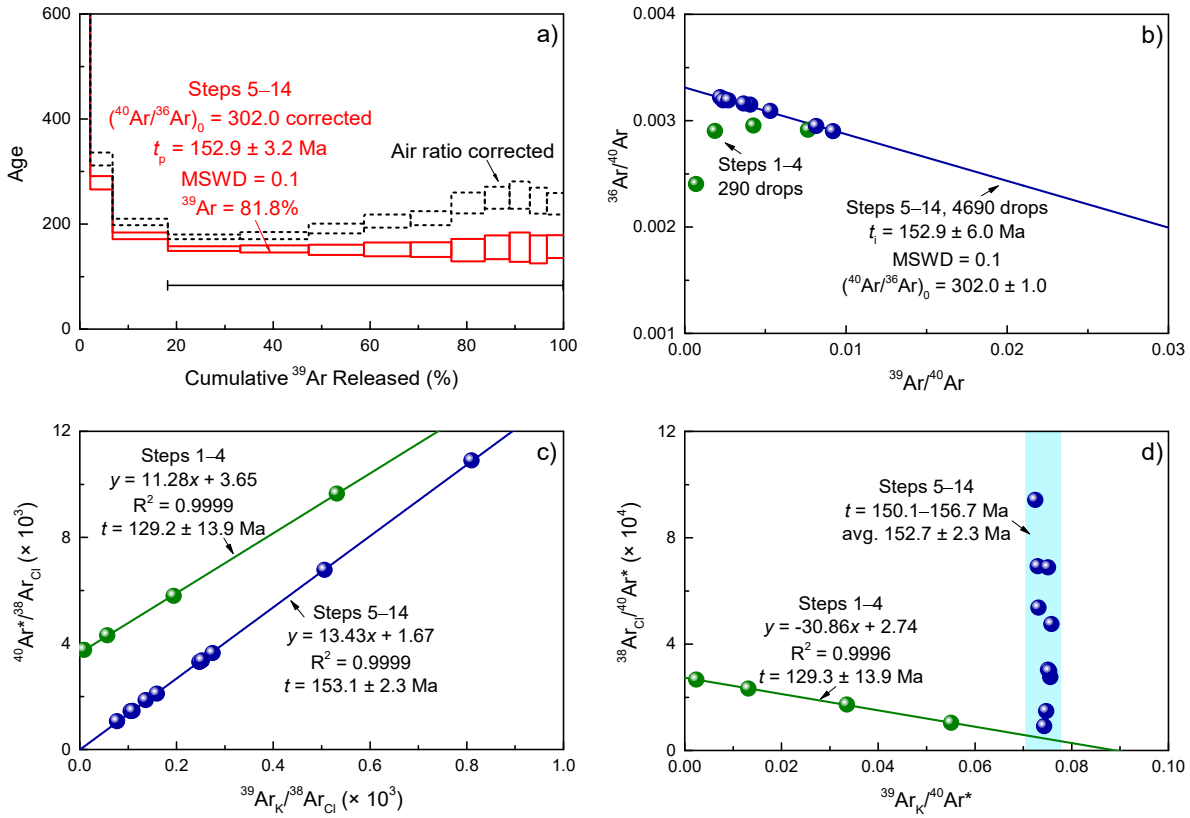

Fig. 10. Fluid inclusion $^{40}Ar/^{39}Ar$ results of the cassiterite sample 13YGX32Cst. (a) Age spectrum. The plateau age (solid red line) was calculated by assuming trapped initial $^{40}Ar/^{36}Ar$ ratio of 302.0. The range of the corrected age, i.e., 147–158 Ma, which is derived from the intercept (302.0 ± 1.0), is not shown in the age spectrum. The black dotted line represents air ratio (295.5) corrected age spectrum. (b) Inverse isochron diagram. The pestle drop numbers and error ellipses are presented in the inverse isochron diagram. (c–d) Correlation diagrams of $^{38}Ar_{Cl}$, $^{39}Ar_K$, and $^{40}Ar^*$ (air corrected radiogenic argon). $^{38}Ar_{Cl}$, $^{39}Ar_K$ were produced by neutron-induced reactions from Cl, and K, respectively. The ages of the final steps were calculated using the initial $^{40}Ar/^{36}Ar$ ratio of 302.0, and the other steps were calculated using the atmospheric ratio (295.5) to exclude non-radiogenic argon. (For interpretation of the references to colour in this figure legend, the reader is referred to the web version of this article.)

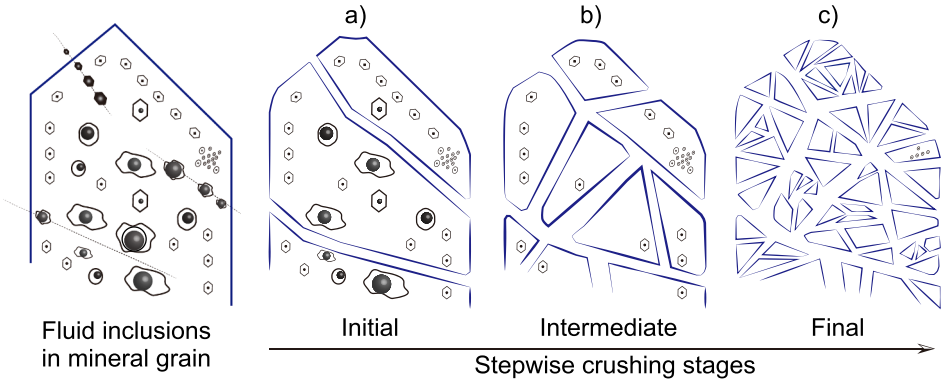

Fig. 11. Sketch map showing the breakup process of mineral grains and the degassing process of mineral-hosted fluid inclusions during stepwise crushing.

of the irradiated cassiterite sample, gases released from initial crushing steps 1–4 (290 drops of crushing) yielded a good linear correlation between $^{38}Ar_{Cl}$ and $^{40}Ar^*$ (see Fig. B.1 in Appendix B). Previous $^{40}Ar/^{39}Ar$ studies have suggested that chlorine and excess argon are closely associated in the fluids (Kelley et al., 1986; Turner and Wang, 1992; Jiang et al., 2012; Bai et al., 2013, 2019). The correlation between $^{38}Ar_{Cl}$ and excess ^{40}Ar can be regarded as an indicator of fluid inclusion degassing (Turner and Wang, 1992; Harrison et al., 1994; Bai et al., 2013). These initial crushing steps of the cassiterite also yielded isochron ages of *ca.* 129 Ma based on their Cl–K–Ar correlations (Fig. 10c–d). These ages are similar to the SFI ages (128–127 Ma) of spatially associated quartz and cassiterite samples as well as the stepwise heating $^{40}Ar/^{39}Ar$ age (129.2 ± 2.1 Ma) of a late crosscutting K-feldspar vein in that sample from the same ore deposit as reported by Xiao et al. (2019). Given the high proportions of formamide and CO_2 in the gases released during the first several crushing steps of its unirradiated counterpart (Fig. 7b), these extractions most likely represent the degassing of large, irregular, and formamide-bearing Type II SFIs in the sample. Large vapors of these SFIs could be the most important reservoir for excess argon in the mineral. Gases released from these SFIs could have resulted in high $^{40}Ar^*$

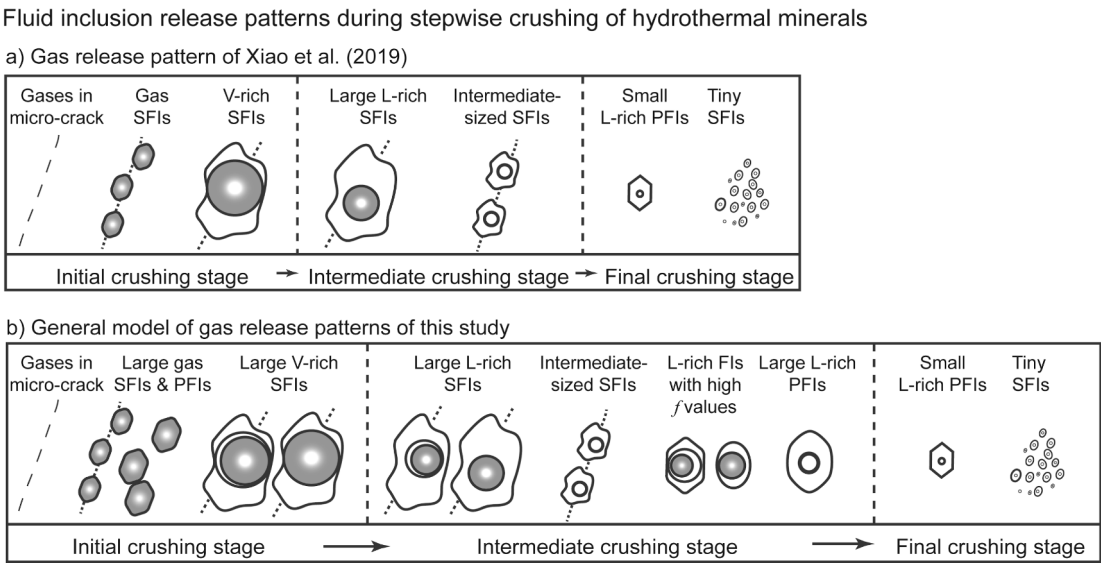

Fig. 12. Gas release patterns during stepwise crushing of hydrothermal minerals. (a) Gas release pattern concluded by Xiao et al. (2019). (b) Updated general model of gas release patterns by this study.

contents (Fig. B.2, Appendix B) and thus the elevated apparent ages (Fig. 10a) in initial crushing steps. Additionally, stepwise crushing extracts SFIs from high-*f* to low-*f* in general without considering the impact of fluid inclusion sizes and compositions (Fig. 12b). This effect likely generated the low and increasing $^{39}Ar_K$ contents during these crushing steps (Fig. B.2).

It is apparent from the above example that the proposed model of gas release patterns offers important information for more accurate interpretations of $^{40}Ar/^{39}Ar$ geochronological data. The QMS-stepwise crushing experiment of the unirradiated cassiterite sample 13YGX32Cst suggests that very fine SFIs in the sample could be released in the final crushing stage along with the PFIs (Fig. 7b). Given their high abundance, argon derived from these very fine SFIs could cause significant interferences and result in large errors in the PFI $^{40}Ar/^{39}Ar$ ages from the final crushing steps (Fig. 10).

5.2.2. *Implication for tracing fluid origins and processes of mineralization*

While the stepwise crushing technique has been applied in gas composition analysis for decades (Sarda et al., 1985; Trieloff et al., 2000; Hopp et al., 2004; Buikin et al., 2005; Buikin et al., 2014), only a few authors have noticed the potential of this technique in separating gases from different fluid inclusion generations (e.g., Buikin et al., 2016; Xiao et al., 2021). Moreover, there have been few attempts to discriminatively use and explain data derived from different stepwise crushing stages due to the lack of a clear criterion. This gap can be filled by the finding of this work, which can support more accurate data interpretation in terms of constraining the fluid sources and hydrothermal processes that affected a geological system, such as an ore deposit.

For example, as shown in the discrimination diagrams of N_2/Ar–CO_2/CH_4 of Norman and Moore (1999) (Fig. 13, improved by Blamey (2012)), the initial-extracted gases show compositions varying from evolved crustal water (namely meteoric water approximatively in equilibrium with crustal rocks) and/or organic crustal water to magmatic water whereas the final-extracted gases have compositions varying from evolved magmatic water to organic crustal water, which indicates distinct fluid sources these gases have. Based on the petrographic characteristics of fluid inclusions in these minerals (Figs. 3–5) and the proposed general model of gas release patterns during gentle stepwise crushing (Fig. 12b), it is easy to conclude that the initial-extracted gases are mainly derived from SFIs which could form in different episodes of hydrothermal events and have different fluid sources whereas the final-extracted gases are mainly derived from the PFIs which may contain magmatic and crustal non-magmatic components in the source and form in a reduced environment (Fig. 13). Additionally, the secondary gases released in the first several steps of the quartz samples 13YGX32Qtz and 13YGX06Qtz plot in the space of evolved crustal water and close to that of shallow meteoric water (Fig. 13b and c) whereas the primary gases extracted in the final

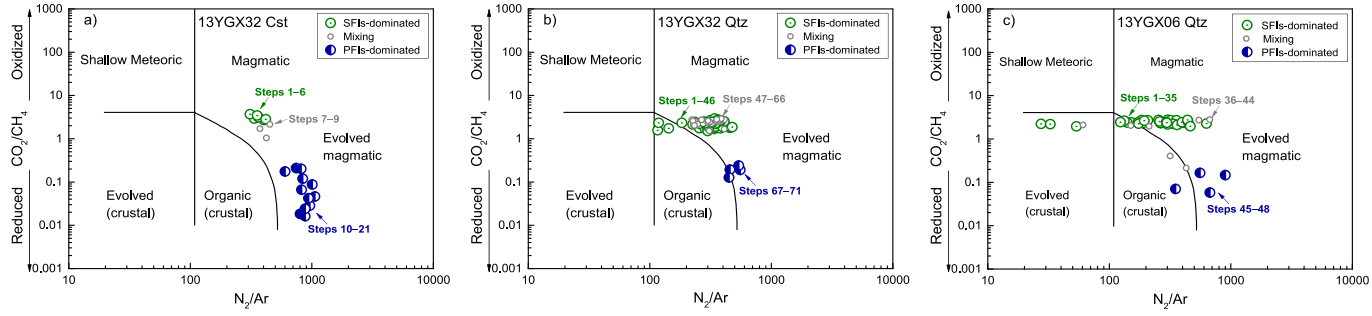

Fig. 13. Plots of N_2/Ar versus CO_2/CH_4 ratios. This discrimination diagram is developed by Norman and Moore (1999) and improved by Blamey (2012) to distinguish fluid origins of volatiles, i.e., magmatic, evolved magmatic, shallow meteoric, crustal, and crustal organic sources. Crustal water represents meteoric fluids approximatively in equilibrium with crustal rocks. Organic crustal water represents meteoric fluids approximatively in equilibrium with crustal rocks and contaminated by organic species derived from wall rocks. Evolved magmatic water represents composite fluids that consist of various proportions of volatiles from magmatic, crustal, and/or meteoric sources.

crushing steps plot away from shallow meteoric water, which indicates the contribution of shallow meteoric water occur during the formation of a certain group of SFIs rather than PFIs (see more details in Xiao et al. (2021)). This result suggests that the conclusion derived from fluid inclusion He–Ar isotope analysis on chalcopyrite, wolframite, pyrite, and arsenopyrite from this deposit that shallow meteoric water contributed to the precipitation of tungsten-tin minerals (Chen et al., 2011; Hu et al., 2012) likely needs reconsideration.

In many situations, if we cannot effectively exclude the influence of SFIs during compositional analysis of fluid inclusion populations, we would not be able to obtain the true ore-forming information. Fortunately, the stepwise crushing technique coupled with the general model of gas release patterns allows us to extract additional information carried by different generations of fluid inclusions. It should be noted that this general gas release model is only applicable in systems where different generations of fluid inclusions have significant physical and/or chemical differences. Random destruction of fluid inclusions during crushing and simultaneous extraction of SFIs and PFIs near microcracks are also unavoidable. However, compared with most traditional extraction methods, this technique permits the extraction of different groups of fluid inclusions with minimal interferences, which can offer better insights into the geological process of the ore deposits.

6. Conclusions

Combined Raman and QMS gas composition analyses of cassiterite and quartz minerals allowed us to build a more detailed model to explain the gas release patterns of fluid inclusions with complicated features during the stepwise crushing experiments of common hydrothermal minerals. The main pieces of the conclusions are summarized below.

1) Microscopic observations coupled with Raman spectroscopic results suggested that many types of fluid inclusions develop in the cassiterite and quartz from ore-bearing quartz veins in the Yaogangxian deposit, e.g., 1) CO_2-rich pure gas inclusions and gas-rich SFIs, 2) large CO_2-bearing tri-phase SFIs and PFIs with variable *f* values, 3) large, irregular and liquid-rich CO_2-rich SFIs along micro-cracks, which usually contain formamide, 4) mid-sized, mid-*f*, CO_2-rich two-phase PFIs, and 5) small, low-*f*, methanoic two-phase PFIs in three-dimensional clusters or along mineral growth zones. Compared with the methanoic PFIs, the CO_2-rich PFIs have larger sizes, more round shapes, higher *f* values, and higher $A(CO_2/CH_4)$ ratios (> 1).
2) QMS analysis of these minerals revealed distinct gas compositions during different stepwise crushing stages, i.e., H_2O-poor and CO_2-rich (CO_2/CH_4 ratios > 1) gases in the initial crushing stage, H_2O- and formamide-rich gases in the intermediate crushing stage, and CH_4-rich (CO_2/CH_4 ratios < 1) gases in the final crushing stage.
3) Combined with the Raman results of different types/generations of fluid inclusions, the differences of gas compositions in different crushing stages suggested that stepwise crushing with gentle crushing strengths progressively extracts secondary gas inclusions and gas-rich SFIs, large liquid-rich SFIs and PFIs with higher *f* values, and small PFIs with lower *f* values. These observations allowed the establishment of a general model of gas release patterns of multi-generations/phases of fluid inclusions during stepwise crushing of common hydrothermal minerals.
4) This updated model distinguishes sources of gases during stepwise crushing and provides more thorough characterizations of the gas composition from each of these sources and more precise PFI composition analysis when combined with detailed petrography and micro-petrography. Therefore, this study provides a better and more general framework for interpreting data generated using gentle stepwise crushing techniques including $^{40}Ar/^{39}Ar$ geochronology, stable isotope, noble gases, and volatile analyses of fluid inclusions.
5) Additionally, we show that the combined QMS-stepwise crushing technique is a reliable analytical technique for gas compositions of multi-phases and multi-generations of fluid inclusions within hydrothermal minerals. Combined with the updated model of gas release patterns, the gentle stepwise crushing technique should have great application prospects in future isotopic and volatile composition analyses.

Data availability statement

The data that support this study are available in the supplementary materials.

Declaration of Competing Interest

The authors declare that they have no known competing financial interests or personal relationships that could have appeared to influence the work reported in this paper.

Acknowledgements

We thank Prof. Jens Hopp and an anonymous reviewer for their constructive comments and suggestions, which greatly improved this manuscript. We appreciate the helpful discussions with Yang Wu, Xiaochun Li, and Ye Wan. This project was supported by the Project funded by China Postdoctoral Science Foundation (No. 2019M663133), the National Natural Science Foundation of China (No. 42022017, 41630315 and 41688103), the Guangdong Basic and Applied Basic Research Foundation (No. 2019A1515012190), the International Partnership Program of Chinese Academy of Sciences (No. 132744KYSB20190039), and the Director's Fund of Guangzhou Institute of Geochemistry, CAS (No. 2019SZJJ-06). NSF grant EAR-1714892 to Yue Cai is also acknowledged.

Appendix A. Supplementary data

Supplementary data to this article can be found online at https://doi.org/10.1016/j.oregeorev.2021.104588.

References

Alderton, D.H.M., Thompson, M., Rankin, A.H., Chryssoulis, S.L., 1982. Developments of the ICP-linked decrepitation technique for the analysis of fluid inclusions in quartz. Chem. Geol. 37 (1), 203–213.
Andrawes, F., Holzer, G., Roedder, E., Gibson, E.K., Oro, J., 1984. Gas chromatographic analysis of volatiles in fluid and gas inclusions. J. Chromatogr. A, A 302, 181–193.
Andrawes, F.F., Gibson, E.K., 1979. Release and analysis of gases from geological samples. Am. Mineral. 64 (3–4), 453–463.
Audétat, A., Günther, D., 1999. Mobility and H_2O loss from fluid inclusions in natural quartz crystals. Contrib. Miner. Petrol. 137 (1–2), 1–14.
Bai, X.J., Hu, R.G., Jiang, Y.D., Liu, X., Tang, B., Qiu, H.N., 2019. Refined insight into $^{40}Ar/^{39}Ar$ progressive crushing technique from K–Cl–Ar correlations in fluid inclusions. Chem. Geol. 515, 37–49.
Bai, X.J., Jiang, Y.D., Hu, R.G., Gu, X.P., Qiu, H.N., 2018a. Revealing mineralization and subsequent hydrothermal events: Insights from $^{40}Ar/^{39}Ar$ isochron and novel gas mixing lines of hydrothermal quartzs by progressive crushing. Chem. Geol. 483, 332–341.
Bai, X.J., Qiu, H.N., Liu, W.G., Mei, L.F., 2018b. Automatic $^{40}Ar/^{39}Ar$ dating techniques using multicollector ARGUS VI noble gas mass spectrometer with self-made peripheral apparatus. J. Earth Sci. 29 (2), 408–415.
Bai, X.J., Wang, M., Jiang, Y.D., Qiu, H.N., 2013. Direct dating of tin-tungsten mineralization of the Piaotang tungsten deposit, South China, by $^{40}Ar–^{39}Ar$ progressive crushing. Geochim. Cosmochim. Acta 114, 1–12.
Bergman, S.C., Dubessy, J., 1984. CO_2-CO fluid inclusions in a composite peridotite xenolith: implications for upper mantle oxygen fugacity. Contrib. Miner. Petrol. 85 (1), 1–13.
Blamey, N.J.F., 2012. Composition and evolution of crustal, geothermal and hydrothermal fluids interpreted using quantitative fluid inclusion gas analysis. J. Geochem. Explor. 116-117, 17–27.
Bodnar, R.J., Samson, I., Anderson, A., Marshall, D., 2003. Reequilibration of fluid inclusions. Fluid Inclusions Anal. Interpretation 32, 213–230.
Buikin, A.I., Kamaleeva, A.I., Migdisova, N.A., 2016. Prospects of the method of stepwise crushing as a source of information on the fluid phase of rocks and minerals. Petrology 24 (3), 303–313.
Buikin, A., Trieloff, M., Hopp, J., Althaus, T., Korochantseva, E., Schwarz, W.H., Altherr, R., 2005. Noble gas isotopes suggest deep mantle plume source of late

Cenozoic mafic alkaline volcanism in Europe. Earth Planet. Sci. Lett. 230 (1–2), 143–162.
Buikin, A.I., Verchovsky, A.B., Sorokhtina, N.V., Kogarko, L.N., 2014. Composition and sources of volatiles and noble gases in fluid inclusions in pyroxenites and carbonatites of the Seblyavr Massif, Kola Peninsula. Petrology 22 (5), 507–520.
Burke, E.A.J., 2001. Raman microspectrometry of fluid inclusions. Lithos 55 (1–4), 139–158.
Campione, M., Malaspina, N., Frezzotti, M.L., 2015. Threshold size for fluid inclusion decrepitation. J. Geophys. Res. Solid Earth 120 (11), 7396–7402.
Cao, X.F., Lv, X.B., He, M.C., Niu, H., Du, B.F., Mei, W., 2009. An infrared microscope investigation of fluid inclusions in coexisting quartz and wolframite: A case study of Yaogangxian quartz-vein wolframite deposit. Mineral Deposits 28 (5), 611–620 (in Chinese with English abstract).
Chen, H.W., Hu, R.Z., Peng, J.T., Bi, X.W., 2011. Helium and argon isotopic compositions of ore-forming fluid from the Yaogangxian Tungsten Deposit and their geological implications. Acta Mineral. Sin. 31 (3), 597–603 (in Chinese).
Chen, J., Wang, R.C., Zhu, J.C., Lu, J.J., Ma, D.S., 2013. Multiple-aged granitoids and related tungsten-tin mineralization in the Nanling Range, South China. Sci. China Earth Sci. 56 (12), 2045–2055.
Chen, Y.R., 1988. Geological and geochemical characteristics and diagenetic-minerogenetic processes of Yaogangxian granite. Mineral Resour. Geol. 2 (1), 62–72 (in Chinese with English abstract).
Chen, Y.R., 1992. Analysis of the control factors and conditions of the mineralization in Yaogangxian orefield, Yizhang County, Hunan. Hunan Geol. 11 (4), 285–293 (in Chinese with English abstract).
Deng, X.D., Luo, T., Li, J.W., Hu, Z.C., 2019. Direct dating of hydrothermal tungsten mineralization using in situ wolframite U-Pb chronology by laser ablation ICP-MS. Chem. Geol. 515, 94–104.
Dong, S.H., Bi, X.W., Hu, R.Z., Chen, Y.W., Chen, H., 2011. Characteristics of ore-forming fluid in Yaogangxian quartz-vein wolframite deposit, Hunan Province. J. Mineral. Petrol. 31 (2), 54–60 (in Chinese with English abstract).
Fang, C., Qiu, H.N., Zhang, W.F., Xiao, M., Xie, J.J., Bai, X.J., 2018. Quadrupole mass spectrometer analysis of fluid inclusion gases from the Hetai Gold Deposit, Guangdong, Southern China. Geochimica 47 (2), 141–148 (in Chinese with English abstract).
Frezzotti, M.L., Tecce, F., Casagli, A., 2012. Raman spectroscopy for fluid inclusion analysis. J. Geochem. Explor. 112 (1), 1–20.
Frost, R.L., Kristóf, J., Horváth, E., Theo Kloprogge, J., 2001. Raman microscopy of formamide-intercalated kaolinites treated by controlled-rate thermal analysis technology. J. Raman Spectrosc. 32 (10), 873–880.
Gamo, T., Glasby, G.P., 2003. Submarine hydrothermal activity in coastal zones. In: Taniguchi, M., Wang, K., Gamo, T. (Eds.), Land and Marine Hydrogeology. Elsevier, Amsterdam, pp. 151–163.
Goldstein, R.H., Reynolds, T.J., 1994. Systematics of fluid inclusions in diagenetic minerals. SEPM Short Course (Soc. Sediment. Geol.) 31, 199.
Hall, D.L., Bodnar, R.J., 1989. Comparison of fluid inclusion decrepitation and acoustic emission profiles of Westerly granite and Sioux quartzite. Tectonophysics 168 (4), 283–296.
Harrison, T.M., Heizler, M.T., Lovera, O.M., Chen, W., Grove, M., 1994. A chlorine disinfectant for excess argon released from K-felsspar during step heating. Earth Planet. Sci. Lett. 123 (1–4), 95–104.
Hopp, J., Trieloff, M., 2005. Refining the noble gas record of the Réunion mantle plume source: Implications on mantle geochemistry. Earth Planet. Sci. Lett. 240 (3–4), 573–588.
Hopp, J., Trieloff, M., Altherr, R., 2004. Neon isotopes in mantle rocks from the Red Sea region reveal large-scale plume–lithosphere interaction. Earth Planet. Sci. Lett. 219 (1–2), 61–76.
Hu, R.Z., Bi, X.W., Jiang, G.H., Chen, H.W., Peng, J.T., Qi, Y.Q., Wu, L.Y., Wei, W.F., 2012. Mantle-derived noble gases in ore-forming fluids of the granite-related Yaogangxian tungsten deposit, Southeastern China. Mineral. Depos. 47 (6), 623–632.
Hua, R., Chen, P., Zhang, W., Liu, X., Lu, J., Lin, J., Yao, J., Qi, H., Zhang, Z., Gu, S., 2003. Metallogenic systems related to Mesozoic and Cenozoic granitoids in South China. Sci. China, Ser. D Earth Sci. 46 (8), 816–829.
Jiang, Y.D., Qiu, H.N., Xu, Y.G., 2012. Hydrothermal fluids, argon isotopes and mineralization ages of the Fankou Pb-Zn deposit in south China: Insights from sphalerite $^{40}Ar/^{39}Ar$ progressive crushing. Geochim. Cosmochim. Acta 84, 369–379.
Jourdan, F., Matzel, J.P., Renne, P.R., 2007. ^{39}Ar and ^{37}Ar recoil loss during neutron irradiation of sanidine and plagioclase. Geochim. Cosmochim. Acta 71 (11), 2791–2808.
Ke, Y.K., 1998. Handbook of Analytical Chemistry (Part III): Spectral Analysis, second ed. Chemical Industry Press, Beijing.
Kelley, S., Turner, G., Butterfield, A.W., Shepherd, T.J., 1986. The source and significance of argon isotopes in fluid inclusions from areas of mineralization. Earth Planet. Sci. Lett. 79 (3–4), 303–318.
Kendrick, M.A., Miller, J.M., Phillips, D., 2006. Part II. Evaluation of ^{40}Ar–^{39}Ar quartz ages: Implications for fluid inclusion retentivity and determination of initial $^{40}Ar/^{36}Ar$ values in Proterozoic samples. Geochim. Cosmochim. Acta 70 (10), 2562–2576.
Koppers, A.A.P., 2002. ArArCALC—software for $^{40}Ar/^{39}Ar$ age calculations. Comput. Geosci. 28 (5), 605–619.
Landis, G.P., Snee, L.W., Juliani, C., 2005. Evaluation of argon ages and integrity of fluid-inclusion compositions: stepwise noble gas heating experiments on 1.87 Ga alunite from Tapajós Province, Brazil. Chem. Geol. 215 (1-4), 127–153.
Lees, A.J., Straughan, B.P., Gardiner, D.J., 1981. Electrolyte—formamide interactions studied by Raman spectroscopy. J. Mol. Struct. 71, 61–70.
Li, S.T., Wang, J.B., Zhu, X.Y., Wang, Y.L., Han, Y., Guo, N.N., 2011. Chronological characteristics of the Yaogangxian composite pluton in Hunan Province. Geol. Explor. 47 (2), 143–150 (in Chinese with English abstract).
Li, W.S., Ni, P., Wang, G.G., Yang, Y.L., Pan, J.Y., Wang, X.L., Chen, L.L., Fan, M.S., 2020. A possible linkage between highly fractionated granitoids and associated W-mineralization in the Mesozoic Yaogangxian granitic intrusion, Nanling region, South China. J. Asian Earth Sci. 193, 104314. https://doi.org/10.1016/j.jseaes.2020.104314.
Lin, X.D., Zhang, D.H., Zhang, C.L., 1986. A discussion on the property of ore-forming fluid of the wolframite quartz-vein in the Yaogangxian tungsten deposit, Yizhang County, Hunan Province. Earth Sci. J. China Univ. Geosci. 11 (02), 153–160 (in Chinese with English abstract).
Liu, M., Qiu, H.N., Bai, X.J., Xiao, M., He, L.Y., 2018. Quadrupole mass spectrometer method in analysis of the gas compositions of fluid inclusions. Geotectonica Et Metallogenia 42 (2), 1–9 (in Chinese with English abstract).
Lowell, R.P., Kolandaivelu, K., Rona, P.A., 2014. Hydrothermal Activity☆, Reference Module in Earth Systems and Environmental Sciences. Elsevier.
Mao, J.W., Cheng, Y.B., Chen, M.F., Pirajno, F., 2013. Major types and time–space distribution of Mesozoic ore deposits in South China and their geodynamic settings. Miner. Deposita 48 (3), 267–294.
Mao, J., Pirajno, F., Cook, N., 2011. Mesozoic metallogeny in East China and corresponding geodynamic settings—an introduction to the special issue. Ore Geol. Rev. 43 (1), 1–7.
Matsumoto, T., Chen, Y., Matsuda, J.I., 2001. Concomitant occurrence of primordial and recycled noble gases in the Earth's mantle. Earth Planet. Sci. Lett. 185 (1–2), 35–47.
Norman, D.I., Moore, J.N., 1999. Methane and excess N_2 and Ar in geothermal fluid inclusions, Proceedings: Twenty-fourth Workshop of Geothermal Reservoir Engineering. Stanford University, Stanford, California, pp. 233–240.
Norman, D.I., Sawkins, F.J., 1987. Analysis of volatiles in fluid inclusions by mass spectrometry. Chem. Geol. 61 (1–4), 1–10.
Paine, J.H., Nomade, S., Renne, P.R., 2006. Quantification of ^{39}Ar recoil ejection from GA1550 biotite during neutron irradiation as a function of grain dimensions. Geochim. Cosmochim. Acta 70 (6), 1507–1517.
Partamies, S.A.G., Poutiainen, M.A.J., 2001. Application of acoustic fluid inclusion decrepitometry to gold exploration in Finland. Geochem. Explor. Environ. Anal. 1 (2), 109–117.
Pecher, A., 1981. Experimental decrepitation and re-equilibration of fluid inclusions in synthetic quartz. Tectonophysics 78 (1–4), 567–583.
Peng, J., Zhou, M.F., Hu, R., Shen, N., Yuan, S., Bi, X., Du, A., Qu, W., 2006. Precise molybdenite Re–Os and mica Ar–Ar dating of the Mesozoic Yaogangxian tungsten deposit, central Nanling district, South China. Mineral. Deposita 41 (7), 661–669.
Pirajno, F., 2008. Hydrothermal processes and mineral systems. Springer Science & Business Media.
Pironon, J., Pagel, M., Lévêque, M.H., Mogé, M., 1995. Organic inclusions in salt. Part I: Solid and liquid organic matter, carbon dioxide and nitrogen species in fluid inclusions from the Bresse basin (France). Org Geochem. 23 (5), 391–402.
Puranik, P.G., Ramiah, K.V., 1959. Infrared and Raman spectroscopic studies of the association of formamide. J. Mol. Spectrosc. 3 (1-6), 486–495.
Qiu, H.N., Jiang, Y.D., 2007. Sphalerite $^{40}Ar/^{39}Ar$ progressive crushing and stepwise heating techniques. Earth Planet. Sci. Lett. 256 (1–2), 224–232.
Qiu, H.N., Wijbrans, J.R., 2006. Paleozoic ages and excess ^{40}Ar in garnets from the Bixiling eclogite in Dabieshan, China: New insights from $^{40}Ar/^{39}Ar$ dating by stepwise crushing. Geochim. Cosmochim. Acta 70 (9), 2354–2370.
Qiu, H.N., Wu, H.Y., Yun, J.B., Feng, Z.H., Xu, Y.G., Mei, L.F., Wijbrans, J.R., 2011. High-precision ^{40}Ar–^{39}Ar age of the gas emplacement into the Songliao Basin. Geology 39 (5), 451–454.
Qiu, H.N., Zhu, B.Q., Sun, D., 2002. Age significance interpreted from ^{40}Ar–^{39}Ar dating of quartz samples from the Dongchuan Copper Deposits, Yunnan, SW China, by crushing and heating. Geochem. J. 36 (5), 475–491.
Ren, Z., Vasconcelos, P.M., 2019. Quantifying ^{39}Ar recoil in natural hypogene and supergene alunites and jarosites. Geochim. Cosmochim. Acta 260, 84–98.
Roedder, E., 1984. Fluid inclusions, 12. Mineralogical Society of America, 644 pp.
Roedder, E., 1997. Fluid inclusion studies of hydrothermal ore deposits. In: Barnes, H.L. (Ed.), Geochemistry of Hydrothermal Ore Deposits. Wiley and Sons Inc., New York, pp. 657–698.
Sarda, P., Staudacher, T., Allègre, C.J., 1985. $^{40}Ar/^{36}Ar$ in MORB glasses: constraints on atmosphere and mantle evolution. Earth Planet. Sci. Lett. 72 (4), 357–375.
Scarsi, P., 2000. Fractional extraction of helium by crushing of olivine and clinopyroxene phenocrysts: Effects on the $^{3}He/^{4}He$ measured ratio. Geochim. Cosmochim. Acta 64 (21), 3751–3762.
Scott, H.S., 1948. The decrepitation method applied to minerals with fluid inclusions. Econ. Geol. 43 (8), 637–654.
Seitz, J.C., Pasteris, J.D., Chou, I.-M., 1996. Raman spectroscopic characterization of gas mixtures; II, quantitative composition and pressure determination of the CO_2-CH_4 system. Am. J. Sci. 296 (6), 577–600.
Shi, K.T., Wang, K.Y., Yu, H.J., Wang, Z.G., Ma, X.L., Bai, X.J., Wang, R., 2018. The $^{40}Ar/^{39}Ar$ dating of quartz: new insights into the metallogenic chronology of the Jinchang gold deposit and its geological significance. Scientific Reports, 8: Article Number: 13879.
Shu, L.S., 2007. Geological Setting of the Nanling Range. Genesis of Late Mesozoic Granites and Lithospheric Evolution in the Nanling Range. Science Press, Beijing.
Simmons, S.F., 2021. Geothermal Resources. In: Alderton, D., Elias, S.A. (Eds.), Encyclopedia of Geology, second ed. Academic Press, Oxford, pp. 708–722.
Singh, T.B., Rey, L., Gartia, R.K., 2011. Applications of PeakFit software in thermoluminescence studies. Indian J. Pure Appl. Phys. 49 (5), 297–302.

Staudacher, T.h., Sarda, P.h., Richardson, S.H., Allègre, C.J., Sagna, I., Dmitriev, L.V., 1989. Noble gases in basalt glasses from a Mid-Atlantic Ridge topographic high at 14 N: geodynamic consequences. Earth Planet. Sci. Lett. 96 (1-2), 119–133.
Steiger, R.H., Jäger, E., 1977. Subcommission on geochronology: convention on the use of decay constants in geo-and cosmochronology. Earth Planet. Sci. Lett. 36 (3), 359–362.
Stuart, F., Turner, G., Duckworth, R.C., Fallick, A., 1994. Helium isotopes as tracers of trapped hydrothermal fluids in ocean-floor sulfides. Geology 22 (9), 823–826.
Stuart, F.M., Turner, G., 1992. The abundance and isotopic composition of the noble gases in ancient fluids. Chem. Geol.: Isotope Geosci. Section 101 (1–2), 97–109.
Tarantola, A., Diamond, L.W., Stünitz, H., Thust, A., Pec, M., 2012. Modification of fluid inclusions in quartz by deviatoric stress. III: influence of principal stresses on inclusion density and orientation. Contrib. Miner. Petrol. 164 (3), 537–550.
Trieloff, M., Kunz, J., Clague, D.A., Harrison, D., Allègre, C.J., 2000. The nature of pristine noble gases in mantle plumes. Science 288 (5468), 1036–1038.
Trieloff, M., Weber, H.W., Kurat, G., Jessberger, E.K., Janicke, J., 1997. Noble gases, their carrier phases, and argon chronology of upper mantle rocks from Zabargad Island, Red Sea. Geochim. Cosmochim. Acta 61 (23), 5065–5088.
Turner, G., Wang, S.S., 1992. Excess argon, crustal fluids and apparent isochrons from crushing K-feldspar. Earth Planet. Sci. Lett. 110 (1–4), 193–211.
Villa, I.M., 2001. Radiogenic isotopes in fluid inclusions. Lithos 55 (1–4), 115–124.
Wang, S.S., 1983. Age determinations of ^{40}Ar–^{40}K, ^{40}Ar–^{39}Ar and radiogenic ^{40}Ar released characteristics on K-Ar geostandards of China. Chin. J. Geol. (4), 315–323 (in Chinese with English abstract).
Wang, Y.L., Pei, R.F., Li, J.W., Qu, W.J., Li, L., Wang, H.L., Du, A.D., 2010. Re–Os dating of molybdenite from the Yaogangxian tungsten deposit, South China, and its geological significance. Acta Geol. Sin. English Ed. 82 (4), 820–825.
Xiao, M., Qiu, H.N., Cai, Y., Jiang, Y.D., Zhang, W.F., Fang, Y., 2021. Progressively released gases from fluid inclusions reveal new insights on W-Sn mineralization of the Yaogangxian tungsten deposit, South China. Ore Geol. Rev. 138, 104353.
Xiao, M., Qiu, H.N., Jiang, Y.D., Cai, Y., Bai, X.J., Zhang, W.F., Liu, M., Qin, C.J., 2019. Gas release systematics of mineral-hosted fluid inclusions during stepwise crushing: implications for $^{40}Ar/^{39}Ar$ geochronology of hydrothermal fluids. Geochim. Cosmochim. Acta 251, 36–55.
Yardley, B.W.D., Bodnar, R.J., 2014. Fluids in the continental crust. Geochem. Perspect. 3 (1), 1–127.
Yuan, S.D., Williams-Jones, A.E., Romer, R.L., Zhao, P.L., Mao, J.W., 2019. Protolith-related thermal controls on the decoupling of Sn and W in Sn-W Metallogenic Provinces: Insights from the Nanling Region, China. Econ. Geol. 114 (5), 1005–1012.
Zhu, X.Y., Wang, Y.L., Cheng, X.Y., Tian, Y., Fu, Q.B., Li, S.T., Yu, Z.F., 2015. Metallogenic system of Yaogangxian quartz vein-type tungsten deposit. Hunan Province Mineral Deposits 34 (5), 874–894 (in Chinese with English abstract).